Building and Environment 307 (2027) 115498

Contents lists available at ScienceDirect

Building and Environment

journal homepage: www.elsevier.com/locate/buildenv

CFD-based multi-objective optimization of vehicle cabin ventilation: trade-off between airborne infection risk and draft discomfort

Bahadir Erman Yuce [a], Yunus Emre Cetin [b,*], Martin Kriegel [b]

[a] Department of Air Conditioning and Refrigeration Technology, Yenişehir İbrahim Orhan Vocational School, Bursa Uludağ University, 16900, Bursa, Türkiye
[b] Hermann-Rietschel-Institut, Technische Universität Berlin, Marchstraße 4, 10587, Berlin, Germany

ARTICLE INFO

Keywords:
Vehicle cabin
Cross-contamination
Comfort
CFD
Multi-objective optimization

ABSTRACT

Vehicle cabins are key microenvironments for airborne disease transmission, owing to their confined spaces and high occupant density. Ventilation that reduces infection risk often causes drafts, creating a dilemma between health protection and thermal comfort. This study addresses the trade-off between airborne cross-infection risk and thermal comfort, expressed as the draft rate (DR), through multi-objective optimization. Numerical analysis used the standard k-ε turbulence model, validated against particle image velocimetry data, and N_2O tracer transport, with duct-informed vent inlet profiles from a two-stage simulation. Four tracer species, one per occupant, released simultaneously, resolved all 12 source-receptor cross-infection pathways through a cell-wise Wells-Riley model; draft was quantified by the cabin-averaged and worst-seat DR. A Taguchi L27 array with Grey Relational Analysis (GRA) consolidated the 13 conflicting responses into a Grey Relational Grade (GRG), 90.3% of whose variance was due to inlet velocity. The predicted optimum, 9 m/s and 12°C with nominal vent angles of 60°, 0°, 60° and 60°, was confirmed by a direct simulation (GRG 0.941; predicted 0.922 ± 0.099) and by runs varying Vent 1 and Vent 2 at fixed velocity and temperature. It reduces the mean infection probability to 1.5%, 94% below the worst case, but at cabin-averaged and worst-seat DRs of 82.8% and 99.3%, far beyond ISO 7730 Category III; the same layout at 20°C has the highest grade of all runs (0.946), with a cabin-averaged DR of 67.7% at unchanged infection risk. Both are temporary high-dilution modes, not comfortable operating points.

1. Introduction

Vehicles like buses, trains, planes, and cars create micro-indoor spaces that are highly critical for the spread of airborne diseases. The confined spaces and limited passenger capacity in vehicles bring people into close proximity for extended periods, increasing the infection risk [1–3]. Pandemic history also supports this: on a cruise ship, 25% of passengers were infected [4,5], and during a bus ride, the infection rate was about 35% [6].

Vehicle cabins are inherently high-risk microenvironments for the spread of airborne diseases because of their unique physical constraints, which are often examined in the context of thermal comfort and air quality analysis [7,8]. The most critical feature of these environments is the relatively small passenger compartment volume; for example, the air volume of a medium-sized car cabin can be as small as about 2.3 m^3 [9]. In this confined space, the presence of the driver and passengers creates high passenger density, increasing the risk of rapid accumulation and high concentrations of respiratory aerosols in the cabin air. This, combined with the asymmetrical and highly non-uniform airflow inside the cabin, creates an environment that makes it difficult for aerosols to disperse effectively due to large-scale recirculation flows [9] and complex eddy structures [10] where the Heating, Ventilation and Air Conditioning (HVAC) system mixes cold air. Consequently, vehicle cabins are challenging microenvironments where the transport of airborne particles is dense, thereby increasing the infection risk [11].

Ventilation strategies with high supply velocity implemented to improve air quality in vehicle cabins and indirectly reduce the risk of infection increase cabin air velocities, creating significant "thermal discomfort" and "draft risk" for passengers. A literature study reported that when ventilation jets are directed at the passenger's chest area, Effective Draft Temperature (EDT) values drop below -4 °C due to high velocity and low temperature, causing significant local discomfort [12]. Similarly, in some strategies that provide air supply from the ceiling, a strong draft sensation occurs when airflow is directed directly at the driver's head at 1.1 m/s, impairing comfort [13]. Innovative diffusers with lobed vanes can provide smoother air distribution, reducing the

* Corresponding author.
E-mail address: y.cetin@tu-berlin.de (Y.E. Cetin).

https://doi.org/10.1016/j.buildenv.2026.115498
Received 12 June 2026; Received in revised form 15 October 2026; Accepted 27 October 2026
Available online 28 October 2026
0360-1323/© 2026 The Authors. Published by Elsevier Ltd. This is an open access article under the CC BY license (http://creativecommons.org/licenses/by/4.0/).
Open access funding enabled and organized by Projekt DEAL.

effects of high-velocity jets and the draft sensation [14]. The vehicle cabin's thermal comfort was studied extensively using CFD. Warey et al. [15] coupled high-fidelity CFD with machine learning to predict occupant comfort across a wide range of HVAC and environmental conditions, deriving indices such as PMV and PPD, and Reda et al. [16] used PMV and PPD to compare different supply configurations. At the same time, increasing airflow can reduce the amount of airborne pathogens inside the cabin. However, this creates a difficult trade-off: high rates of exchange for combating infection or rapid cooling conflict with passenger comfort, which requires lower airflow rates.

In recent literature, many studies have focused on airborne transmission in the vehicle cabin. Nabilou et al. [17] used a respiratory manikin to study the distribution of respiratory particles smaller than 1 micron in a passenger car cabin. Their data showed that the seat behind the infected person had the highest risk of particle exposure, while the seat to the side had the lowest. In a study by Pan et al. [18], methods to reduce the risk of infection for a taxi driver with infected passengers were investigated using computational fluid dynamics and LES-Lagrangian models. The study found that opening the windows, installing interior partitions, and using far-UVC lamps significantly reduced exposure to respirable particles. The authors presented a scenario in which the windows are left half-open and the air conditioning flow is set to a specific setting as the optimal solution. Beyond these cases, Arpino et al. [19] analyzed transient, non-isothermal aerosol dispersion in a two-occupant car cabin and showed that the HVAC system operation mode and the occupant seating position strongly govern the contaminant distribution, while Arpino et al. [20] combined an emission-to-risk approach with a validated CFD model and found that the SARS-CoV-2 infection probability during a 30-min trip varies from near zero to about 50%, depending mainly on the HVAC flow rate, and that zero-dimensional well-mixed approaches are inadequate for such confined spaces. Kim et al. [21] examined the ventilation efficiency of air conditioning and open windows in a sedan and a cutaway bus using aerosol concentration measurements. The findings showed that the highest efficiency was achieved in a moving vehicle with all windows open, with 80% of aerosols removed per minute in the sedan. Wells-Riley modeling indicated that a 10% infection probability was reached in 1.2 minutes in an unventilated sedan, while opening all windows while in motion extended this time to 32 minutes.

In addition, other recent studies focused on more crowded transport spaces. Yan et al. [22], in a three-row Boeing 737 section, showed that a passenger's cough jet breaks up the ascending thermal plumes of seated occupants and locks contaminants into the local environments of neighbouring passengers, with residence times up to 50% longer and travel distances nearly doubled for particles up to 200 μm, the jet's influence lasting about 4 s, eight times the cough itself. Their results show that, in dense seating, exposure is a seat-level rather than a cabin-level quantity, which is the premise of our twelve-pathway formulation; it also motivates our stated limitation that continuous breathing, not transient coughing, is modeled here. Li et al. [23], in the Airbus A320 flight deck, a compartment closer to a driver's position than any passenger cabin, found that the windshield inlets created a near-field vortex that locked contaminants around the pilot and that an outlet located ahead of the pilot raised the pilot's exposure above the co-pilot's. Exposure was governed by the inlet-outlet arrangement around one seat, which is the role that register orientation plays as a design factor in our study, and the pilot/co-pilot asymmetry is the counterpart of the left/-right asymmetry we find between driver and front passenger. Qin et al. [24], in a polar cruise-ship cabin, evaluated four ventilation systems against thermal comfort and air quality simultaneously, used the draft rate as the local comfort index, and found that the only system meeting comfort in both seasons did so at a 6% energy penalty and a 49% increase in mean age of air. This is the same trade-off structure as ours, assessed with the same comfort index, in a comparably low and crowded cabin.

The assessment of infection risk was extended from single cars to buses and other enclosed transport environments. Cao et al. [25] compared cars and buses under different ventilation settings and found, using a local infection-risk measure, that the probability of infection for passengers in small cars can exceed that in large buses. Applying the Wells-Riley model to their measurements, Kim et al. [21] also showed that the infection probability depends strongly on the air-circulation method and the vehicle type.

An analysis of the latest research trends suggests that the most prominent tool for simulating airflow, heat distribution, and the spread of particulate matter in vehicle cabin space is Computational Fluid Dynamics (CFD) [7]. In these simulations, the Reynolds-averaged Navier-Stokes equations are used to model fluid turbulence, and the mass, momentum, and energy balance equations (RANS) are solved. In simulations of pollutant spread, which are essential for evaluating infection risks, the numerical Species Transport model [26] or the Tracer Gas method [27] can be used. Taken together, these studies have treated aerosol dispersion, infection risk, and thermal comfort largely as separate problems. However, one of the most important gaps in the methodologies used for the simulation of the infection risks and thermal comfort of the occupants of vehicles, as identified by the literature, is the scarcity of research studies focusing on the optimization of thermal comfort and infection risks simultaneously, and the evaluation of the tradeoff between the two important factors in the optimization process. Furthermore, there is a lack of a body of work that incorporates multi-objective optimization and statistical techniques, such as Grey Relational Analysis (GRA) integrated with the Taguchi method, to effectively address the complex interactions among system parameters and identify optimal conditions for system performance. Population-based metaheuristics such as genetic algorithms, particle swarm optimization and the grey wolf optimizer have been applied to indoor-environment design, but they require hundreds to thousands of objective evaluations, which is prohibitive when each evaluation is a three-dimensional CFD solution; the Taguchi-GRA route adopted here reaches a compromise solution with 27 runs, at the cost of searching only a discrete level grid (Section 4). Lastly, while several studies have assessed airborne infection risk in vehicle cabins, they typically consider a single contaminant source, most often the driver or one passenger [20], and do not resolve all occupant-to-occupant transmission pathways within a fully occupied cabin or couple this multi-source risk assessment with draft-comfort considerations in a multi-objective optimization.

Relative to the cabin studies cited above, the present work resolves all twelve occupant-to-occupant pathways simultaneously rather than a single source; applies the Wells-Riley exponent cell by cell rather than to a cabin-averaged concentration; couples the multi-source risk field to a draft objective in one optimization; treats the four registers as independent factors, which is what makes an asymmetric optimum discoverable; and supplies the registers with duct-informed inlet profiles, with the optimum confirmed and its register effects separated by direct simulations.

To address these identified gaps, the present study introduces a comprehensive framework that simultaneously optimizes airborne cross-infection risk (via the Wells-Riley model) and thermal comfort (via the Draft Rate) within a vehicle cabin. The principal contributions of this work are threefold: (i) a local, CFD-coupled Wells-Riley formulation that replaces the well-mixed assumption with spatially resolved quanta concentrations and is applied to a fully occupied cabin, with all four occupants acting simultaneously as independently tagged contaminant sources, so that all twelve occupant-to-occupant transmission pathways are resolved in a single solution; (ii) the first systematic analysis of all 12 source-receptor cross-infection pathways in a fully occupied vehicle cabin, treating each of the four occupants as a potential infection source; and (iii) a hybrid Taguchi-GRA multi-objective optimization that reduces 13 conflicting performance indicators to a single Grey Relational Grade, identifying an asymmetric vent configuration, confirmed by direct simulations with duct-informed inlet profiles, as the optimal high-

dilution ventilation mode. The novelty of this work lies not in the local risk model alone but in resolving all occupant-to-occupant transmission pathways in a fully occupied cabin and integrating this multi-source risk assessment with a draft-based comfort objective within a single multi-objective optimization.

2. Materials and methods

In this study, a general SUV cabin model was used to simulate basic airflow and thermal characteristics. The computational model was also equipped with detailed manikin models of the driver, front passenger, and two rear passengers (rear left and rear right). The cabin envelope is about 2.6 meters long, 1.5 meters wide, and 1.2 meters high, and the enclosed air volume, excluding the manikins and seats, is 2.34 m^3. Ventilation is provided by four dashboard vents: the side vents, Vent 1 (driver side) and Vent 4 (passenger side), measure 80.2 mm × 75.0 mm and 82.0 mm × 73.8 mm, and the central vents, Vent 2 and Vent 3, 84.0 mm × 75.0 mm each (0.0247 m^2 in total). The luggage rack features two exhaust outlets, each measuring 300 mm x 20 mm. The geometric model is shown in Fig. 1.

The numerical simulations in this research were done using ANSYS Fluent 2025 R1 with the finite volume method (FVM). Three-dimensional steady-state analysis was applied to simulate the processes of airflow, heat transfer, and species transport within the cabin. All governing equations, such as the continuity, momentum, energy, radiation, and species transport equations, were solved simultaneously as steady state equations. The density was obtained from the incompressible ideal-gas law, i.e. from the local temperature and mixture composition at the operating pressure, so that the buoyancy forces caused by temperature differences within the passenger compartment follow directly from the computed temperature field, without the Boussinesq approximation; the density of the cabin air ranged from 1.08 to 1.24 kg/m^3 in all simulations.

The standard k-ε turbulence model with standard wall functions and

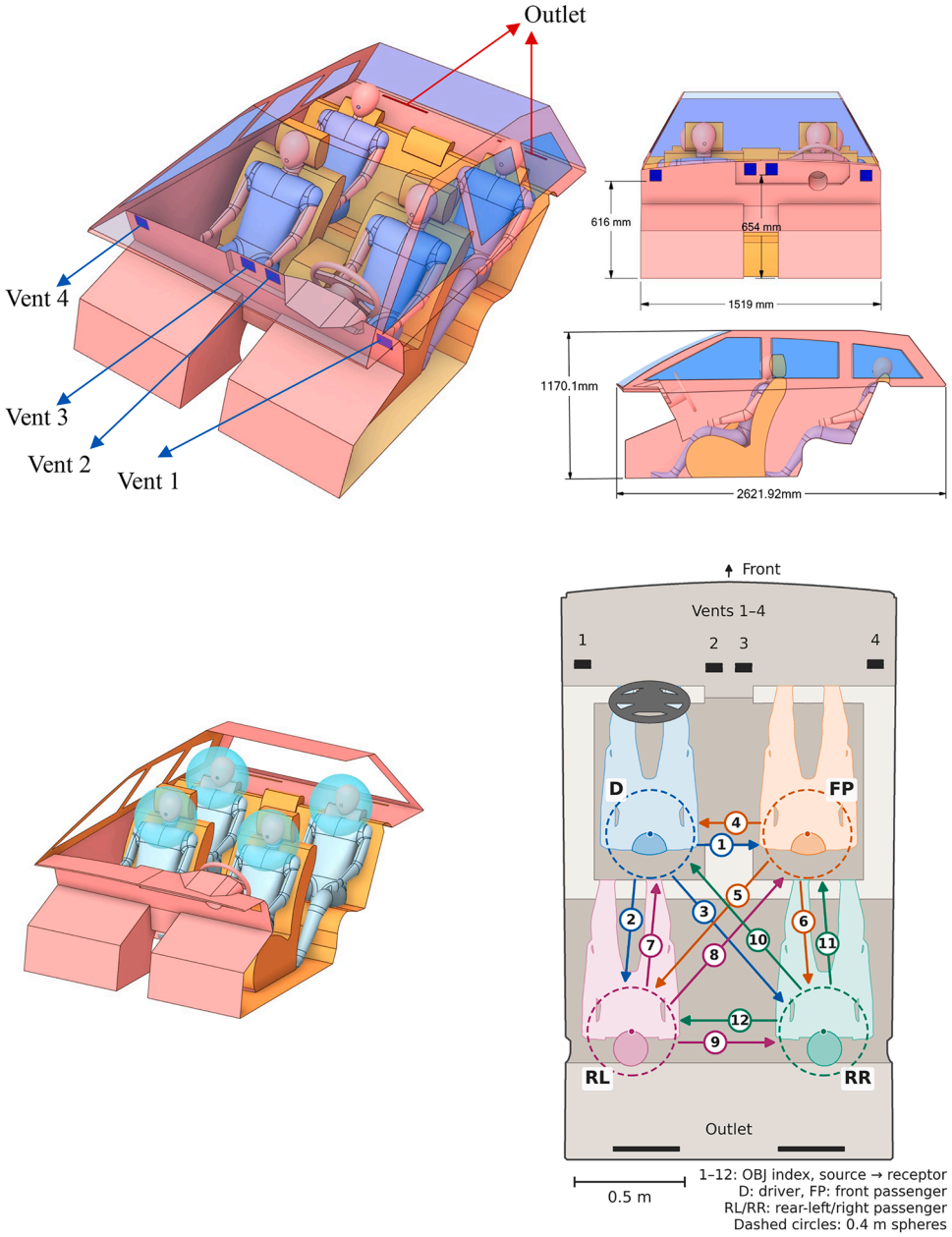

Fig. 1. The computational domain of the vehicle cabin, including the locations of inlet vents, outlet openings, and the four occupants, the volumes for N_2O mass fraction and infection risk calculation for each passenger and driver, and transmission pathways for each OBJ index.

curvature correction [28] was used for all cabin simulations (model constants $C_\mu = 0.09$, $C_{1\varepsilon} = 1.44$, $C_{2\varepsilon} = 1.92$, $\sigma_k = 1.0$ and $\sigma_\varepsilon = 1.3$; turbulent Prandtl number 0.85), and the validation case, which will be presented in detail in the following sections, was solved with the same model. On the manikin surfaces the mean y^+ is 1.7-2.0 at 1 m/s, 3.8-5.7 at 5 m/s and 6.1-9.6 at 9 m/s (95th percentiles 3.9-30); where y* falls below 11.225, the standard wall function applies the laminar stress-strain relationship [28], so that the fine near-wall cells are treated consistently.

The pressure-based coupled solver with pseudo-transient relaxation was used, with second-order interpolation for pressure, the second-order upwind scheme for momentum, energy, density and species transport, and the first-order upwind scheme for the turbulent kinetic energy (k) and its dissipation rate (ε). The cabin flow does not settle to a single steady state but oscillates about a stationary mean; the infection probabilities of the last iteration differ from their iteration averages by a factor between 0.43 and 1.40 (5th-95th percentiles). All responses are therefore iteration averages: after 500 warm-up iterations (1000 for the out-of-array runs of Section 3.6), the responses were sampled every 20 iterations over 1000 iterations (51 samples; the point values of Section 2.4, from which the worst-seat DR is obtained, every 100 iterations), and their standard error was estimated from five consecutive batch means. The standard error is at most 8.3% of the range of the respective response over the 27 cases and at most 0.0056 for the grey relational grade; the responses and their standard errors are listed in Table S1. An iteration average of the pseudo-transient steady solution is a numerical average rather than a time average of the unsteady flow, which is a further reason for the scale-resolving simulations planned in Section 4.

2.1. Modeling of exposure

The Species Transport model was used to examine the distribution of tracer gas within the cabin [29]:

$$\frac{\partial}{\partial t}(\rho Y_i) + \nabla.(\rho \vec{v} Y_i) = -\nabla.\vec{J}_i + R_i + S_i \quad (1)$$

In Eq. 1, ρ is the fluid density, Y_i is the local mass fraction, $\vec{v}$ is the velocity vector, R_i is the net rate of production, $\vec{J}_i$ is the diffusion flux of tracer gas, and S_i is the rate of the source.

Compared to other occasional respiratory activities such as sneezing or coughing, human exhaled breaths have the potential to contain the largest number of droplets and the largest volume of air in total [30], and according to the findings of Ma et al., COVID-19 patients release SARS-CoV-2 directly into the air through the breathing [31].

Papineni and Rosenthal analyzed droplets expelled by humans performing four respiratory actions using an optical particle counter and found that most particles were smaller than 1 μm, though larger particles were also present [32]. Bivolarova et al. measured aerosol particles of various sizes (0.07, 0.7, and 3.5 μm) along with N_2O tracer gas in a room with mixing ventilation. Their research showed that N_2O emerged as a reliable predictor of exposure to all tested different-sized particles [33]. Li et al. used CFD to demonstrate that particles smaller than 2.5 μm and the distribution of CO_2 tracer gas exhibited very similar spatial patterns [34,35]. According to these studies in the literature, the tracer gas approach was adopted in this study to examine the airborne pathogen distribution and infection risk estimation.

In this study, the infected individual's steady breathing throughout the journey was modeled instead of sudden actions such as coughing or sneezing. The vast majority of particles exhaled during quiet breathing are respiratory aerosols under 5 μm [36] in diameter. These particles tend to follow cabin airflow rather than settle under gravity. Based on this physical behavior, N_2O was selected as the tracer gas to represent virus-laden aerosols.

The fine aerosols that dominate quiet breathing have negligible gravitational settling velocities (below approximately 0.8 mm/s for a 5-micrometer droplet) and very small Stokes numbers at the air velocities encountered in the cabin, so they follow the airflow with negligible slip and can be represented as a passive scalar. Accordingly, the present Eulerian tracer-gas approach represents the long-range airborne aerosol route that dominates cross-cabin transmission, and does not reproduce the inertia, gravitational settling, or evaporation of larger droplets, whose ballistic, settling-dominated behavior is confined to short-range near-source deposition; resolving this large-droplet contribution would require an Eulerian-Lagrangian model with droplet evaporation and a realistic size distribution, which is identified as a complementary future direction.

One simulation was performed per case. All four occupants exhale simultaneously in every case, and four chemically distinct tracer species (one per occupant) are transported in the same solution, so that the twelve source-receptor pathways are separated by species rather than by separate runs; the four scenarios discussed in Section 3 are post-processing views of one solution, and each pathway is evaluated for the realistic situation in which all occupants breathe. With a mouth area of 3.1-3.2 cm^2 and 6.0-6.2 L/min, each exhalation jet exits at 0.32 m/s with a momentum flux of about 6×10^{-5} N, about two to four orders of magnitude below a single supply register; the mouths are 0.6-0.8 m apart and the jets decay within a few diameters, so they do not impinge on one another, and their interaction with the occupants' thermal plumes in the breathing zone is resolved. The tracer is released as pure N_2O at 36°C (1.73 kg/m^3), which is denser than the cabin air, whereas real exhaled air is slightly lighter. This density excess is confined to the vicinity of the mouth: at 9 m/s the volume-averaged tracer mass fraction is 1-5% between 2 and 4 cm from the mouth and below 1.3% beyond 4 cm, and at 1 m/s, where the dilution is weakest, it is 11-13% between 2 and 4 cm and approaches the cabin mean of 3.5% within 16 cm, so that the tracer of a source is transported as a passive scalar when it reaches the breathing zones of the other occupants.

To analyze the potential infectiousness of each of the four passengers in the cabin (four different scenarios) in a single analysis and to differentiate cross-contamination risks, a separate tracer type (N_2O driver, N_2O front passenger, N_2O rear right passenger, N_2O rear left passenger) was assigned to each passenger. Infection risk calculation, which will be defined in detail in the following sections, was calculated in a sphere with a 400 mm diameter centred at the mouth of each receptor, as shown in Fig. 1.

The mouth surface of each manikin (3.1-3.2 cm^2) was defined as the velocity inlet to simulate exhalation. A constant velocity of 0.32 m/s was applied through the mouth, giving 6.0-6.2 L/min, which corresponds to the respiratory minute volume of an adult at rest. Because the Wells-Riley model is integrated over the two-hour journey, the time-averaged concentration field governs the cumulative dose, and the continuous exhalation reproduces this average without resolving the individual breathing cycle. Moreover, since the scaling factor fixes the quanta emission rate (Section 2.3), the flow rate determines mainly the exhalation-jet momentum, which is well below that of the ventilation supply and therefore does not control the in-cabin dispersion. Transient, high-momentum respiratory events such as coughing and sneezing lie outside the continuous-breathing scenario considered here and are addressed in future time-resolved simulations. The temperature of this exhaled air was defined as 36°C, close to body core temperature. Because the N_2O is released at a constant rate while the cabin is continuously ventilated through the outlets, the contaminant does not build up over time; instead, its concentration settles to a statistically stationary level once the amount entering at the source equals the amount leaving through the outlets. The ventilation flow rates replace the cabin air within 2-4 minutes even at 1 m/s (Section 2.2), much faster than the two-hour journey, so this stationary state is reached well within the exposure time.

2.2. Boundary conditions

The boundary conditions of the numerical simulations were determined by considering the requirements of the Taguchi experimental design and the physical reality of summer conditions. Four vent surfaces that provide cabin air conditioning were designated velocity inlets. The air inlet velocity and temperature at these surfaces were varied in the optimization study, with values of 1, 5, and 9 m/s and 12, 16, and 20 °C, respectively. The inlet velocity is the magnitude of the nominal jet velocity of a vent, whose direction is set by the vent angle; the mass flow rate of each vent is therefore $\rho VA \cos\theta$, where A is the vent area and θ the angle between the jet direction and the vent normal (28.7°, 31.3° and 61.3° for the 0°, 60° and 90° settings). A uniform velocity at this flow rate, as commonly used in cabin studies, conserves the supply rate but not the structure of the vent jet [37]. Realistic, duct-informed or measured inlet profiles improve the reproduction of the near-vent jet [37,38]; because the vent angles are design factors, all simulations use duct-informed inlet profiles at the same flow rates (Section 2.2.1).

The levels were chosen to span three distinct flow regimes: 1 m/s is buoyancy-dominated, 9 m/s momentum-dominated and 5 m/s intermediate. Because the flow rate of each vent depends on its angle, the total supply rate is 43-78 m^3/h at 1 m/s, 296-385 m^3/h at 5 m/s and 533-692 m^3/h at 9 m/s (Table S2), corresponding to 18-33, 127-165 and 228-296 air changes per hour of the 2.34 m^3 cabin air volume. The comparison with real vehicles is made on the flow rate, because the cabin air volume of the model excludes the occupants and seats and is smaller than the gross interior volumes of the production cars measured in [39] (3.3-4.7 m^3). Knibbs et al. [39] measured outdoor-air supply rates of 225-300 m^3/h in six stationary cars at the second-highest fan setting and 271-399 m^3/h at 60-110 km/h, and Fruin et al. [40] reported air change rates of up to about 145 h^{-1} at the highest fan setting. The 5 m/s level therefore lies within the measured operating range of passenger-car HVAC units, whereas the 9 m/s level is at or beyond the upper end of their capacity and marks an upper bound of the design space rather than a routine operating point; the consequences are discussed in Section 3.6. 12°C is a moderate supply temperature (face-vent discharge temperatures down to about 2°C occur in maximum cooling [41]), and 20°C a mild supply at the upper end of summer cooling operation. The cabin is ventilated with outside air throughout; the recirculation mode in which in-car air exchange rates are lowest is not represented.

The turbulence quantities at the vents are part of the duct-informed profiles (Section 2.2.1); the uniform-inlet reference solutions of Section 3.7 used a turbulence intensity of 5% and a length scale of 0.01 m. Air discharge is provided through the openings (20 mm x 300 mm) on the rear luggage shelf, designated as "Pressure Outlets," and set to a gauge pressure of 0 Pa; no backflow occurred at the outlets in any simulation.

The thermal boundary conditions were designed to account for both internal loads from human metabolism and external loads from solar radiation and ambient heat exchange. The surfaces of the four manikins in the cabin (skin and clothing, 0.78-0.80 m^2 per manikin) were modeled as walls with a constant heat flux of 80 W/m^2, i.e. 62-64 W per occupant, of the order of the sensible heat release of a seated adult. The buoyant plume is thus generated at its source within the steady RANS framework, so that its mean upward convective transport of heat and of the exhaled tracer is represented, while the instantaneous plume meandering and intermittent shedding are not resolved. The influence of this mean buoyant transport on contaminant migration is examined through the supply-temperature factor, which governs the cabin-to-supply temperature difference and whose contribution is largest for the rear-source pathways (Sections 3.4 and 3.5). Heat exchange with the external environment was represented using a mixed thermal boundary condition that combined convection and external radiation, applied to all enclosure surfaces (windshield, side windows, roof, floor, console, and doors). A convective heat transfer coefficient of 10 W/(m^2 K) was specified, with a free-stream temperature of 30 °C and an external radiation temperature of 30 °C, and zero wall thickness, since the thermal resistance of the thin panels is negligible relative to the external convective heat transfer. The external surface emissivity was 0.88 for the glazed surfaces (windshield and side windows) and 0.95 for the non-glazed surfaces (roof, floor, console, and doors). A no-slip condition applies to the manikins and cabin interior surfaces due to fluid dynamics.

Because the density follows from the ideal-gas law, no Boussinesq approximation is involved. The manikin surface temperature results from the heat-flux condition: its maximum ranges from 41.9 to 58.1°C across the simulations (99th percentile: 32.9-47.2°C), and the maximum air temperature in the cabin ranges from 41.2 to 57.5°C. With the 12°C supply, the largest temperature difference in the domain is therefore about 46 K, which would have exceeded the commonly accepted validity limit of the Boussinesq approximation ($\beta\Delta T \approx 0.1$ [42]) had it been used.

In the simulations, the Surface-to-Surface (S2S) radiation model in the ANSYS Fluent setup computed radiative heat exchange between surfaces using view factors [43]. To account for external solar irradiation and shading, the Solar Ray Tracing method was used. The solar rays were determined using the Solar Calculator, and the coordinates of the Bursa Uludağ University Görükle Campus, where the simulation scenario takes place, were used: 40.22° latitude and 28.87° longitude, corresponding to the summer solstice on June 21 at 13:00 local time. This is a worst-case instantaneous condition, not a journey average; the two-hour Wells-Riley dose is therefore the exposure that would accrue if this steady state persisted, which is the conservative reading for a temporary high-dilution ventilation mode. Because the same solar load is imposed in all cases, its effect is not resolved by the design. The orientation of the simulation domain was defined by setting the North direction as the positive Z-axis (0, 0, 1), the East direction as the negative X-axis (-1, 0, 0), and the direct and diffuse irradiation to 850 W/m^2 and 200 W/m^2, respectively. The spectral fraction, which indicates the distribution of the spectrum between the visible and infrared regions, was set to 0.45. The properties and materials of the cabin's interior and the human body are presented in Table 1 [9,44,45].

2.2.1. Duct-informed inlet profiles

The inlet profiles were obtained with the two-stage approach recommended by Bode et al. [37]. In the first stage, the flow through the face-vent ducts of a passenger-car HVAC module, taken from a publicly available CAD model, was simulated separately (Fig. 2a). The fluid volume (10.73 L) comprises the central Y-duct feeding the two central vents, the two side ducts, their inlet transitions, and a 120 mm × 350 mm × 60 mm volume representing the face outlet of the HVAC unit. Each duct outlet discharges into a rectangular chamber representing the cabin (32 mm margin around the opening, 350 mm long), whose far face is a mass-flow outlet carrying the case's vent flow rate, while the duct inlet is a pressure inlet. The duct model was meshed with 2.4 million tetrahedral cells, converted to polyhedral cells, and solved using the standard k-ε model for the cabin simulations, combined with scalable

Table 1
Material properties [9,44,45].

Component	Material	Density (kg / m^3)	Specific heat (J/ kg K)	Thermal conductivity (W/ m K)
• Windshield • Rear glass • Side glass	Glass [44]	2529.58	754.04	1.1717
• Body • Dashboard • Rear board	ABS plastic [44]	996.35	1480.60	2.70
Seat	Polyurethane foam [44]	70.00	1685.60	0.05
Floor	Carpet [44]	1601.85	1485.38	0.2942
Clothing	Cotton [9]	1297.01	1480.1	0.04
Driver	Skin [45]	1000	3770	0.21

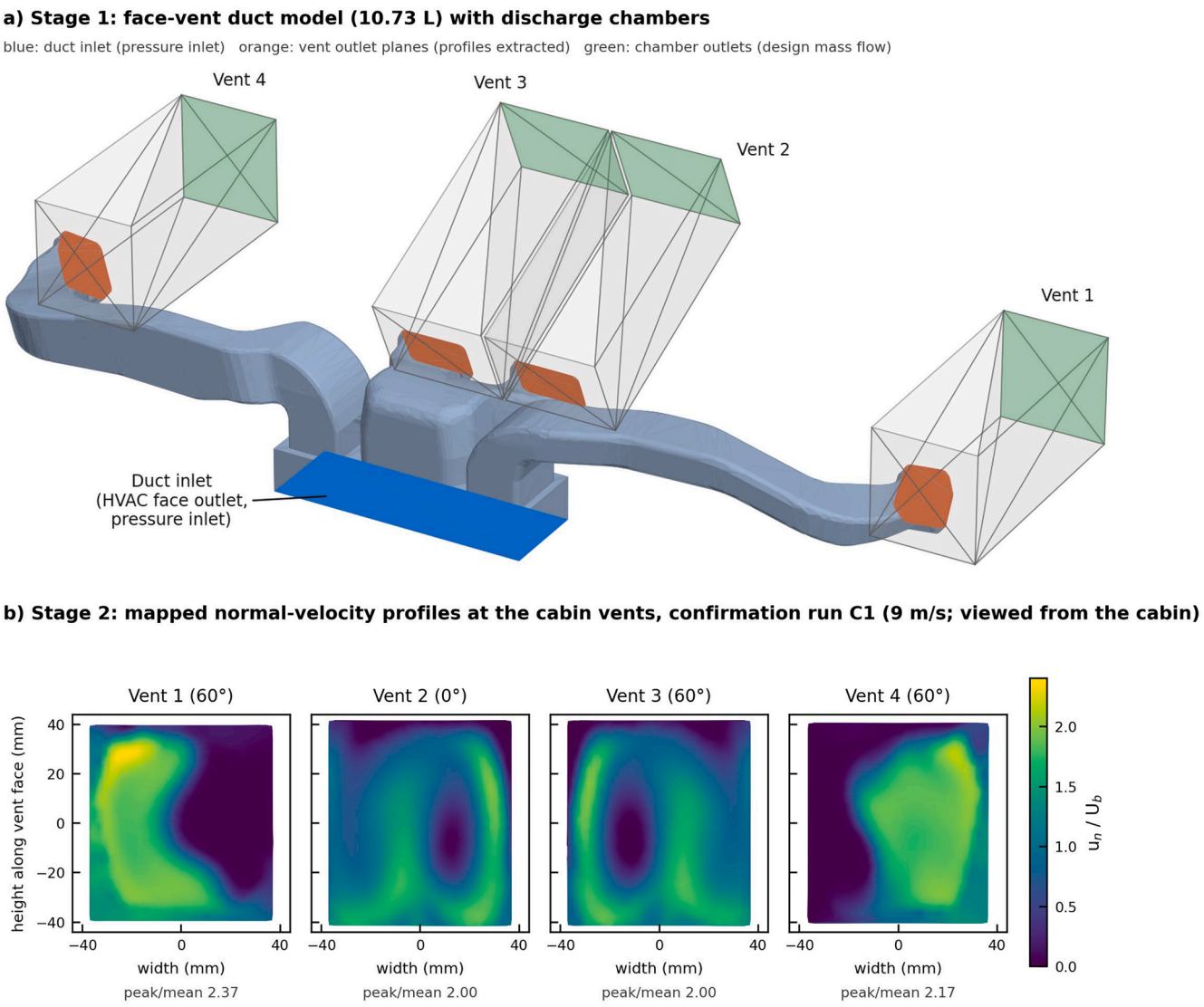

Fig. 2. Duct-informed inlet profiles: a) first stage, face-vent duct model with discharge chambers; b) second stage, normal velocity at the cabin vents in the confirmation run C1 (9 m/s), normalized by the bulk velocity U_b of each vent.

wall functions that avoid the deterioration of standard wall functions on near-wall cells finer than the logarithmic layer. A first-stage simulation was performed with the vent flow rates of each of the 27 cases and of the two further configurations of Section 3.6 (C8 and C9); the remaining out-of-array runs re-used the first-stage solution with the same supply velocity and the same vents at 90°, which determine the flow split between the ducts.

The flow separates in the diffusers that precede the duct outlets (outlet-to-throat area ratio 1.54-1.63) and does not settle to a steady state in RANS, so the vent-exit profiles were averaged: the normal velocity, k and ε were sampled every 10 iterations over windows of 2000-20000 iterations, and the window was extended until the standard error of the mean profile, estimated from ten batch means, fell below 0.015 of the bulk velocity (area-weighted RMS), 0.005 for the jet-direction cosine and 0.5 percentage points for the turbulence intensity at every vent. Two first-stage simulations (Case 22 and C8) reached the 20000-iteration budget with a standard error of 0.020 and 0.019 at one central vent; they were accepted under a limit of 0.03, all other criteria being met.

In the second stage (Fig. 2b), the averaged profiles of the normal velocity, k, and ε were mapped from the duct outlets onto the face centers of the cabin vents by inverse-distance interpolation, after stretching the duct outlets to the vent dimensions (by 0.91-0.94 for the side vents and by 1.36 in height and 0.81 in width for the central vents). The velocity direction at every face is the nominal jet direction of the vent setting, as in a uniform inlet, because the jet direction is set by the vanes, which are not part of the duct model; the duct flow therefore contributes to the spatial distribution of the mass flux and of the turbulence. Faces with reversed flow were set to zero normal velocity (the clipped reversed flow is at most 2.9% of the net vent flow), and each profile was scaled to the flow rate of the case (velocity by s, k by s^2 and ε by s^3). Compared with a uniform inlet at the same flow rate, the mapped profiles have peak-to-mean normal velocities of 1.83-2.40 (median 2.12), momentum fluxes 1.21-1.67 times larger (median 1.42), and turbulence intensities of 4-25% (median 12%) instead of 5% (Table S3).

The sensitivity of the cabin results to the choices made in the first stage was tested for Case 27 by repeating the first-stage simulation with chambers of twice the margin and length (64 mm, 700 mm) and with a duct mesh refined by a factor of 1.5. All 13 optimization responses changed by at most 2.8% of their range across the 27 cases (the cabin-averaged DR by 0.4%), below the 5% criterion set before the comparison. A fully coupled duct-cabin model was not used, because the flow split between the ducts and the jet direction would then be set by the duct resistance and the vane geometry rather than by the design factors, and because the ducts belong to a different vehicle than the generic

cabin.

2.3. Wells-Riley model

The transmission of airborne pathogens and the associated infection risk were calculated using a User-Defined Function (UDF) integrated into the Ansys Fluent solver. While the traditional Wells-Riley model assumes a well-mixed environment, this study used CFD results to obtain a spatial risk distribution based on local concentrations within each computational cell. Although the classical Wells-Riley equation was originally derived for well-mixed indoor environments with uniform pathogen distribution, this assumption leads to significant inaccuracies in confined spaces with strong directional airflows, such as vehicle cabins. To overcome this limitation and capture the spatial heterogeneity of infection risk, this study adopts a local infection probability approach.

A linear relationship was established between the volumetric ratio of N_2O released into the environment, representing the respiratory air of an infected individual, and the infectious dose (quanta) released. In this approach, the mass fraction of N_2O (Y_{N2O}) obtained from the numerical solution was first converted to a volume fraction (X_{N2O}) using the ratio of molecular weights:

$$x_{N2O} = Y_{N2O} \times \frac{MW_{\text{air}}}{MW_{N2O}} \tag{2}$$

In Eq. 2, MW_{air} is the molecular weight of air (28.97 g/mol) and MW_{N2O} is the molecular weight of N_2O (44.01 g/mol). For infection risk calculation, the quanta concentration (C_q, quanta/m^3) in each cell in the simulation area was calculated using a scaling factor (S) derived from the N_2O volume fraction. The scaling factor is defined as the ratio of the assumed amount of quanta (q = 20 quanta/h [46]) emitted by the infected individual to the N_2O volumetric flow rate $\dot{V}_{N2O}$ used to represent the source in the simulation.

$$S = \frac{q}{\dot{V}_{N2O}} \tag{3}$$

$$C_q = S \times x_{N2O} \tag{4}$$

In Eq. 3, $V_{N2O} = 1.0 \times 10^{-4}$ m^3/s (6 L/min) was used; because the mouth flow rates are 6.0-6.2 L/min, the effective emission rates are 20.0-20.5 quanta/h.

The total infectious dose (λ) to which the recipient individual is exposed was calculated based on respiratory rate ($p = 0.5$ m^3/h; seated adult [47]), exposure time (t = 2 h), and local quanta concentration:

$$\lambda = I \times C_q \times p \times t \tag{5}$$

In Eq. 5, I represents the number of infected individuals (1). The inhalation rate p is the value given in [47] for a seated adult; it is independent of the exhalation flow rate of the source, which sets only the jet momentum because the emission rate is fixed by the scaling factor (Section 2.1). Using the calculated lambda value, the local infection probability P_{local} in each calculation cell was determined by the Wells-Riley equation based on the Poisson distribution:

$$P_{\text{local}} = 1 - e^{-\lambda} \tag{6}$$

The objective value of a source-receptor pathway, OBJ, is the volume-weighted average of Plocal of the corresponding tracer over the fluid cells whose centers lie within a sphere of 0.4 m diameter centered at the receptor's mouth: OBJ = Σ_c $P_{\text{local,c}}$ V_c / Σ_c V_c. Because P_{local} is evaluated cell by cell before averaging, OBJ differs from the probability obtained from the sphere-averaged quanta concentration by at most 4.1% (median 0%), whereas the maximum of P_{local} in the sphere is higher by a median of 26%; the optimization with these alternative reductions is reported in Section 3.6.

2.4. Draft rate

This study focuses on Draft Rate (DR) as a single measure of thermal comfort, rather than the commonly used Predicted Mean Vote (PMV) and Predicted Percentage of Dissatisfied (PPD). This choice was made because the study covers the summer season, focuses on cooling, and because DR parameters conflict with infection-risk parameters. In simulated summer conditions in Türkiye, where solar load is high, the vehicle cabin requires high airflow velocities to meet cooling needs and maintain the pathogen-dilution effect. Under these conditions, the primary cause of passenger discomfort is the localized sensation of airflow caused by high-velocity, low-temperature jets impinging on the body.

To assess the local discomfort felt by passengers due to airflow, the DR was used as a thermal comfort index [48]:

$$DR = (34 - t_a)(V - 0.05)^{0.62}(0.37VTu + 3.14) \tag{7}$$

In Eq. 7, V is the velocity (m/s), Tu is turbulence intensity, and t_a is the temperature (°C). DR was evaluated in every cell from the local air temperature, mean speed, and turbulence intensity, Tu = 100·(2k/3)$^{1/2}$/V, where k is the local turbulent kinetic energy; the local mean speed is floored at 0.05 m/s, at which the (V − 0.05) term of Eq. 7 vanishes so that DR = 0 by construction, and DR is capped at 100%, following ISO 7730 [49]; DR is set to zero where the local air temperature exceeds 34°C, where the (34 − ta) term would make it negative. Eq. 7 applies to sedentary subjects near thermal neutrality, at local air temperatures of about 20-26°C, local mean speeds up to about 0.5 m/s, and turbulence intensities of about 10-60% [48,49]. The local speed entering it must not be confused with the vent velocity used as a design factor. The comfort objective entering the optimization is the cabin-averaged DR. Because a volume average is not what an occupant experiences, DR is additionally evaluated at each occupant at 0.10, 0.60 and 1.10 m above the floor, the ankle, abdomen and head heights of a seated person (the uppermost point lies 0.11-0.13 m above the top of the manikin head), from the local temperature, mean speed and turbulence intensity; the seat DR is the mean of the three points and the worst-seat DR the highest seat DR in the cabin. In this cabin, 1.17 m high, the uppermost point lies close to the roof; without it, the seat DR of the rear occupants in C1 remains above 95% because of local speeds of about 2 m/s at 0.60 m (Table 5). The local air temperatures at these points are 27.1-36.4°C at 1 m/s, 20.8-31.4°C at 5 m/s and 18.7-28.7°C at 9 m/s, 8% of the points at 9 m/s lying below 20°C; the local speeds reach 0.25, 1.18 and 2.42 m/s, and only 0%, 23% and 18% of the points at the three velocities satisfy all three validity limits (Table S4). DR is therefore used here as a relative index of draft risk, and values far above the ISO 7730 categories (I < 10%, II < 20%, III < 30% [49]; designated A, B and C before the 2025 revision) indicate a strong draft rather than a calibrated percentage of dissatisfied. Across the 27 cases, the worst-seat DR is correlated with the cabin average (Pearson r = 0.965, Spearman ρ = 0.962) and exceeds it by 11.8 percentage points on average (−3.0 to +41.0 points); a GRA with the worst-seat DR in place of the cabin average is reported in Section 3.6.

2.5. Grid independence study

To confirm that the numerical results were independent of the number of cells, a grid study was conducted with three cell counts: coarse (2.1 million cells), medium (2.4 million cells), and fine (3.4 million cells). The grid study was carried out with the initial model set-up, i.e. with uniform inlet velocities and the standard k-ε model with standard wall functions, before the duct-informed inlet profiles were introduced. The velocity and temperature profiles were calculated in the Y-direction through a vertical line starting from the floor to the ceiling in the cross-sectional plane of the breathing area of the driver's seat.

From Fig. 3, all three meshes capture the same vertical velocity and temperature trends, with moderate local deviations between the coarse

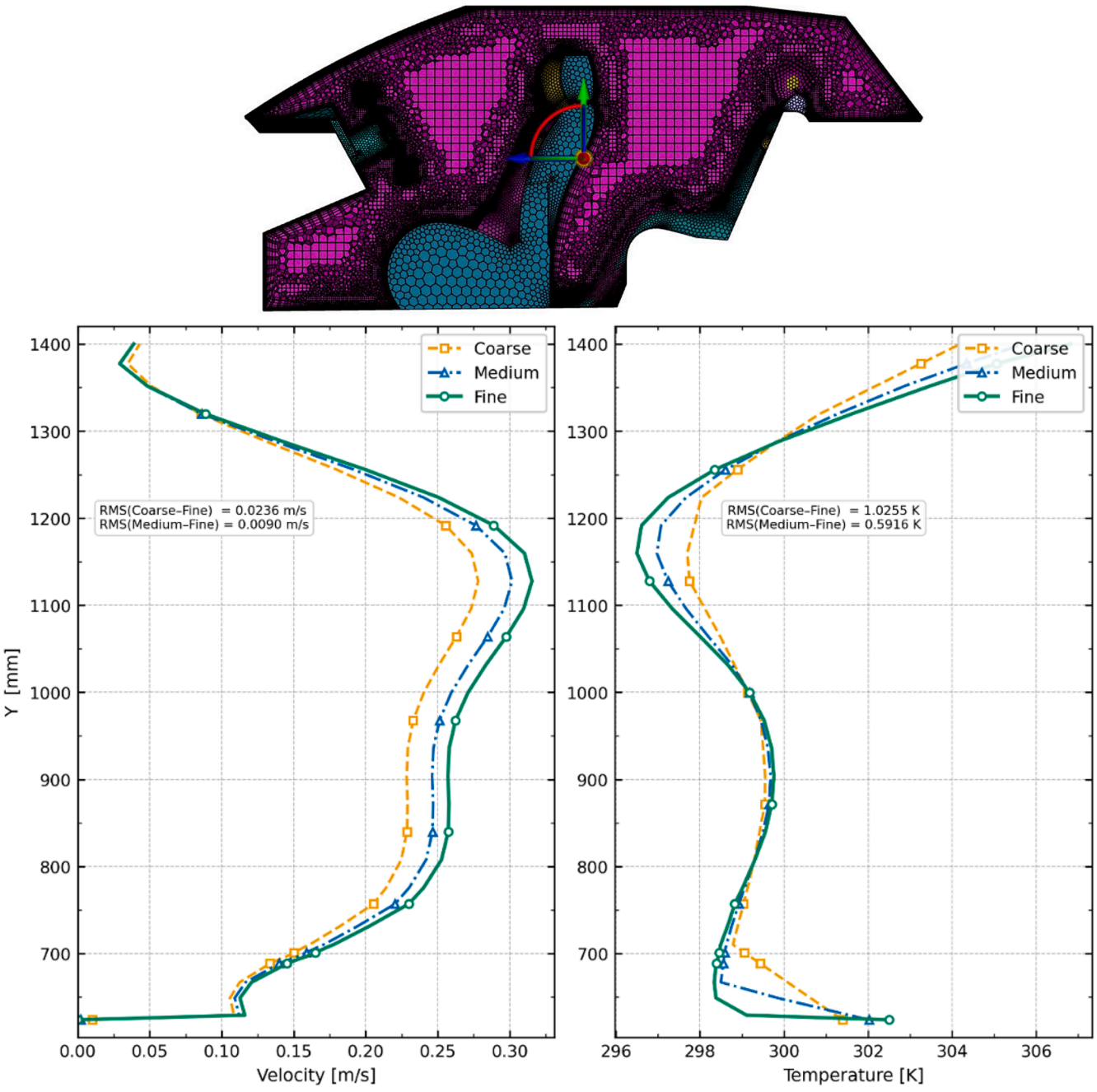

Fig. 3. Mesh and mesh independence study results.

and fine meshes. Regarding velocity, the largest difference occurs in the peak zone, where the airflow from the HVAC system is strongest (Y ≈ 1050-1150 mm). On the other hand, the largest temperature differences occur near the lower and upper boundaries (Y ≈ 650-700 mm and Y > 1300 mm), whereas the medium- and fine-mesh profiles agree closely across the entire height.

Quantitatively, the root mean square (RMS) deviations are defined as:

$$RMS = \sqrt{\frac{1}{N}\sum_{i=1}^{N}\left(U_{\text{mesh},i} - U_{\text{fine},i}\right)^2} \tag{8}$$

For the velocity profile, the RMS deviation between coarse and fine meshes was 0.0236 m/s, while the deviation between the medium and fine meshes decreased to 0.0090 m/s, representing a 62% improvement. For the temperature profile, the RMS between the coarse and fine meshes was 1.0255 K, while the deviation between the medium and fine meshes decreased to 0.5916 K, representing a 42% improvement. Despite this improvement, the absolute temperature deviation between the medium and fine meshes remained below 0.6 K throughout the profile, which is an acceptable value for cabin thermal analysis.

The medium-to-fine deviations of 0.0090 m/s and 0.59 K indicate that the profiles are grid-independent from the medium level onwards. The production simulations used a polyhedral mesh of 2.40 million cells, between the coarse and medium meshes of this study, so that its deviations from the fine-mesh profiles are expected to lie between those of the medium and coarse meshes (RMS 0.009-0.024 m/s and 0.59-1.03 K); the near-wall resolution of this mesh is given in Section 2.

2.6. Validation

The model's velocity field was validated against particle image velocimetry (PIV) measurements by Ozeki et al. [50] in a half-scale compact-car cabin model under isothermal conditions. The validation case was solved with the turbulence model of the cabin simulations (standard k-ε with standard wall functions and curvature correction) on a mesh of 2.4 million polyhedral cells (mean wall y^+ 0.46), and the velocity magnitude was averaged over 2000 iterations. Profiles were sampled along vertical lines at X = 450, 650, 850, and 1050 mm in the PIV plane, 394.5 mm from the model centerline, and are compared in Fig. 4 with the measurements and with a solution obtained with the realizable k-ε model and enhanced wall treatment on the same mesh.

At X = 450 mm, the section closest to the supply opening, the measured jet peak of 2.77 m/s at Z = 416 mm is predicted as 2.63 m/s at Z = 401 mm, i.e. the jet core is about 15 mm too low and slightly too narrow; this station has the largest deviation (RMSE 0.44 m/s). At X = 650 and 850 mm, the jet is mixed, and the profiles agree closely with the measurements (RMSE 0.13 and 0.11 m/s), and at X = 1050 mm, where the flow is governed by the rear-compartment recirculation, the RMSE is 0.13 m/s. Over all 118 PIV points the RMSE is 0.25 m/s, 11% of the mean inlet velocity, against 0.24 m/s for the realizable k-ε solution, which is better at X = 650 mm (0.08 m/s) and worse at X = 1050 mm (0.21 m/s); the standard error of the computed mean profiles (at most 0.003 m/s) is negligible in comparison.

In each section, the model successfully describes the deceleration, lateral spreading, and upward bending of the feed jet, which agrees with the experimental results of Ozeki et al. [50]. This validates the isothermal velocity field, which governs the velocity-dominated results (front-source pathways and the draft objective), with the turbulence model used for all cabin simulations; the buoyancy, radiation, and solar sub-models are not validated here, and the supply-temperature contributions to the rear-source pathways (Sections 3.4 and 3.5) are the results most exposed to this gap (Section 4).

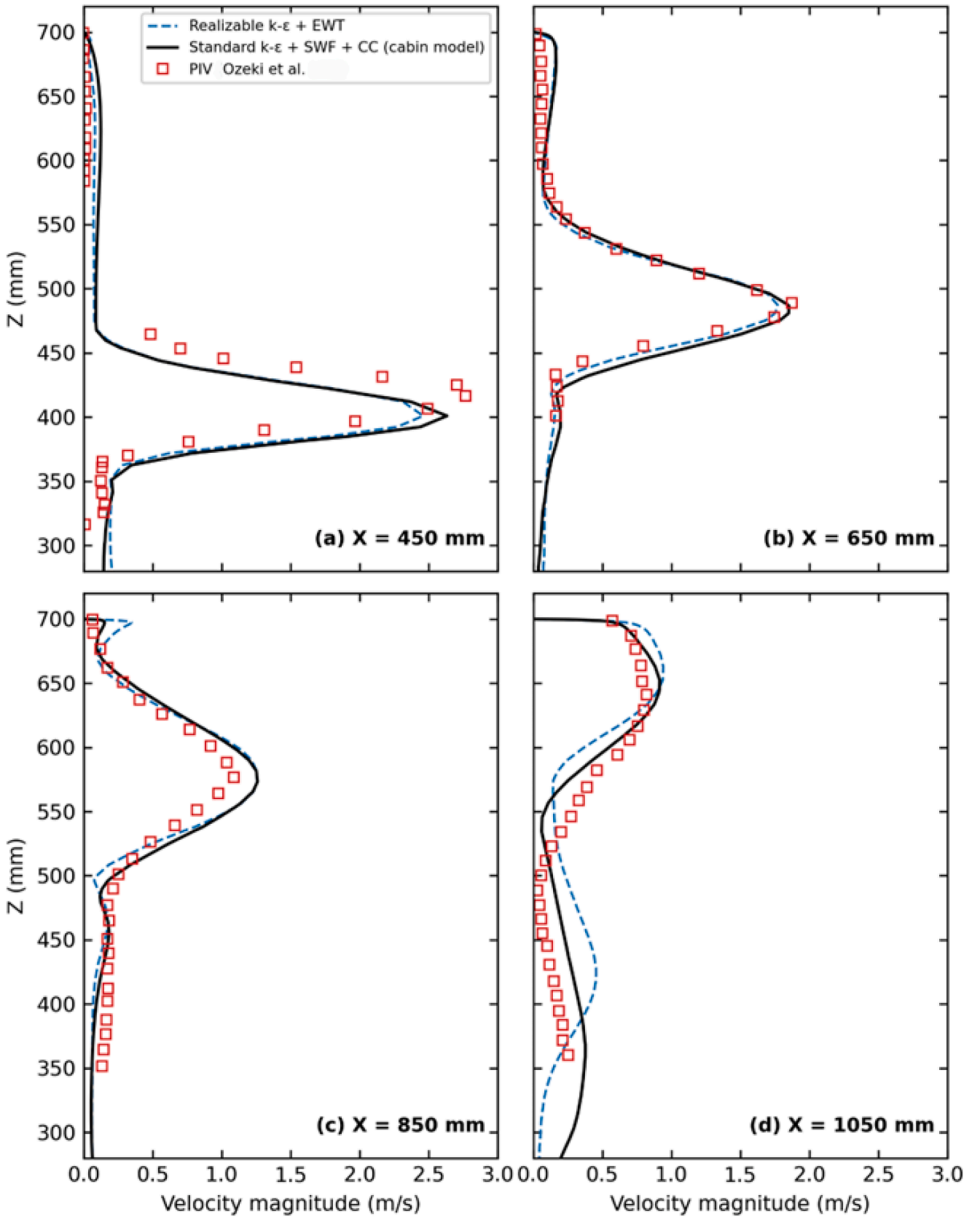

Fig. 4. Velocity magnitude profiles at X = 450, 650, 850 and 1050 mm: PIV measurements of Ozeki et al. [50] and CFD with the turbulence model of the cabin simulations (standard k-ε; band ±2 standard errors of the iteration average, narrower than the line width) and with the realizable k-ε model.

2.7. Taguchi method

This study addresses a multi-objective optimization problem that aims to maximize thermal comfort while minimizing the risk of airborne infection. To this end, the Taguchi method and GRA have been integrated.

The influence of factors (velocity, temperature, vent angle) on a specified problem, as well as the optimal levels of these factors, can be analyzed using the Taguchi method. This method determines the relative importance of independent parameters with respect to dependent objective functions [51] and identifies parameter combinations that yield the best and worst outcomes.

The Taguchi method was used in this study to optimize inlet velocity, temperature, and vent angle to balance airborne infection risk against draft discomfort, quantified by DR. The most important advantage of the Taguchi method is its ability to create a specific experimental design using special orthogonal arrays, which has been used in numerical analyses of contamination, thus significantly reducing the number of experiments required. Since CFD analyses are quite time-consuming, it is not feasible to work parametrically and solve all case combinations. This method, instead of solving all case combinations, reduces the total number of cases by using specific orthogonal arrays and allows the optimal case combination to be obtained. Yuce et al. discussed the advantages and disadvantages of this method in detail [52]. The Taguchi method follows a sequential process. It calculates Signal-to-Noise (S/N) ratios for each factor, determines delta values, and ranks the factors. By using orthogonal arrays, the method efficiently explores the parameter space.

The S/N ratio is defined in three distinct forms: larger is better, lower is better, and nominal is best. In this study, the smaller-is-better form, shown in the equation below, was used for the thirteen responses, and the larger-the-better form for the grey relational grade (Section 2.9):

Smaller the better [53]:

$$\frac{S}{N} = -10log\left(\frac{1}{n}\sum_{i=1}^{n} Y_i^2\right) \quad (9)$$

In Eq. 9, n represents the number of observations per case (here a single simulation) and Y_i is the ith observed value of the performance characteristic. Subsequently, the delta values are computed as the difference between the maximum and minimum S/N ratios for each parameter, enabling subsequent ranking. The parameter with the largest delta value is considered the most important, which helps determine the ranking order. This method was used to find delta values and assign ranks, showing how strongly each parameter affects each response.

In this study, six parameters with three levels, velocity (1, 5, and 9 m/s), temperature (12, 16, and 20 °C), and the angles of four vents (0°, 60°, and 90°; 0° directs the jet horizontally rearwards and 90° vertically upwards), were used. L27 orthogonal array was selected to examine these parameters and their levels in detail, as shown in Table 2. The delta values, detailed in the relevant literature and the main factor in their determination, are included in each Taguchi analysis.

The six factors occupy columns 1-6 of the standard L27(3^{13}) array, with the angle levels coded 1 = 90°, 2 = 60° and 3 = 0°; their main effects use 12 of the 26 degrees of freedom, leaving 14 for the residual. Every level of every factor occurs nine times, and every pair of factors is balanced, each level pair occurring three times. An L9 accommodates at most four three-level factors and could host this design only by lumping the four registers into a single angle factor, which would have made the asymmetric optimum undiscoverable; the L27 reduces the $3^6 = 729$ full factorial by a factor of 27. Because columns 3 and 4 of the L27 carry the interaction of columns 1 and 2, the main effects of A1 and A2 are aliased with the velocity × temperature interaction. In the same assignment, column 6 carries part of the interaction of columns 1 and 5, so that A4 is aliased with the velocity × A3 interaction and A3 with the velocity × A4 interaction, and the temperature main effect is aliased with the velocity × A1 and velocity × A2 interactions; in Cases 1 to 9, A1 equals A2 and A3 equals A4. These are the aliases referred to in Section 4. The predicted optimum is therefore not accepted on the additive prediction alone but confirmed by an independent simulation, and the Vent 1 and Vent 2 effects are separated by direct simulations at fixed velocity and temperature (Section 3.6).

Table 2
L27 Orthogonal Array.

Case No	Velocity (m/s)	Temperature (°C)	A1	A2	A3	A4
1	1	12	90	90	90	90
2	1	12	90	90	60	60
3	1	12	90	90	0	0
4	1	16	60	60	90	90
5	1	16	60	60	60	60
6	1	16	60	60	0	0
7	1	20	0	0	90	90
8	1	20	0	0	60	60
9	1	20	0	0	0	0
10	5	12	60	0	90	60
11	5	12	60	0	60	0
12	5	12	60	0	0	90
13	5	16	0	90	90	60
14	5	16	0	90	60	0
15	5	16	0	90	0	90
16	5	20	90	60	90	60
17	5	20	90	60	60	0
18	5	20	90	60	0	90
19	9	12	0	60	90	0
20	9	12	0	60	60	90
21	9	12	0	60	0	60
22	9	16	90	0	90	0
23	9	16	90	0	60	90
24	9	16	90	0	0	60
25	9	20	60	90	90	0
26	9	20	60	90	60	90
27	9	20	60	90	0	60

2.8. Analysis of variance (ANOVA)

In this research, the analysis of variance (ANOVA) method was not used directly in the optimization process; instead, it was used to discuss and elaborate on the results obtained from the Taguchi method. Using the widely recognized ANOVA method, the experimental outcomes can be comprehensively assessed by quantifying the relative contribution of each parameter. The ANOVA calculation procedure was presented in detail in the literature [52]. For a three-level factor the sum of squares is $SS_F = \Sigma_l n_l (\bar{y}_l - \bar{y})^2$, with $n_l = 9$ and two degrees of freedom; the residual is SS_T minus the six factor sums of squares, with 14 degrees of freedom; and the percentage contribution is $100 \cdot SS_F/SS_T$. Because the design is balanced these contributions are additive and sum to 100%. All ANOVA results are computed on the response values; the full decomposition is given in Table S5. The simulations are deterministic and were not replicated, so the residual represents the unassigned columns of the array and the interactions between factors, not random error; F-tests and p-values are therefore not reported, and the contributions are used descriptively. Because ANOVA operates on the response values, it is dominated by the large infection probabilities at 1 m/s, whereas the logarithmic S/N ratio weights the low-risk cases equally, so the two analyses can rank a secondary factor differently.

2.9. Grey relational analysis (GRA)

Thirteen different outputs obtained from simulations (1 DR and 12 Infection risk probability values from the manikins) were converted into a single "Grey Relational Grade" (GRG) value using the GRA method. Taguchi-based GRA procedure can be defined as below:

1. Normalization: The "smaller-is-better" approach was applied for all infection risk and DR parameters, using the minimum and maximum of each response over the 27 cases of the array; the out-of-array runs of Section 3.6 are graded with the same bounds and weights, so that their grades are directly comparable with those of the array, a response better than the best case of the array giving a coefficient slightly above 1.
2. Optimization: Taguchi Signal-to-Noise (S/N) analysis was performed on the calculated GRG values to determine the optimum parameter set that best balances infection risk and airflow discomfort; the larger-the-better form, which for a single value reduces to S/N = 20 $\log_{10}$(GRG), was used, and the optimum is the level combination that maximizes both the mean GRG and its S/N ratio.

To address the limitations of the Taguchi method, GRA is employed to solve a multi-objective problem [54] simultaneously, using the same set of parameters.

While the Taguchi method focuses on evaluating how parameters affect a single problem, GRA first assesses the relationships among these parameters. Then, ANOVA and the Taguchi method are applied to the GRA results to identify key parameters, determine the optimal scenario, and identify which factors most strongly affect the solution. GRA involves four main steps: (1) normalizing data for each case, (2) calculating the Grey Relational Coefficient (GRC), (3) deriving weight factors, and (4) calculating the Grey Relational Grade (GRG). These steps are detailed in the literature [52]. In the GRA method, weights are considered separately for each objective using delta values as shown in Eq. 10:

$$w_k = \frac{\sum_{j=1}^{p} \Delta_{kj}}{\sum_{k=1}^{m}\sum_{j=1}^{p} \Delta_{kj}} \tag{10}$$

In Eq. 10, Δ is the S/N ratio range, p is the number of parameters, and m is the number of responses.

Each response is normalized as $x_i(k) = (\max y(k) - y_i(k))/(\max y(k) - \min y(k))$; the grey relational coefficient is $GRC_i(k) = (\Delta_{min} + \zeta\Delta_{max})/(\Delta_i(k) + \zeta\Delta_{max})$ with $\Delta_i(k) = 1 - x_i(k)$, $\Delta_{min} = 0$, $\Delta_{max} = 1$ and $\zeta = 0.5$; and the grade is $GRG_i = \Sigma_k\, w_k\, GRC_i(k)$, where i denotes the case, k the response and w_k the weight of response k from Eq. 10. The resulting weights assign 9.3% to the draft-rate objective and 90.7% collectively to the twelve infection objectives, partly because there are twelve of them and partly because they respond more strongly to the factors, so the grade is dominated by infection risk by construction; a weighting sensitivity is reported in Section 3.6. The normalized values, grey relational coefficients, and grades for the 27 cases and the out-of-array runs, the weights, and the S/N ratios of the GRG are listed in Table S6. The additive prediction of the GRG at the optimum is the overall mean plus the deviations of the optimal level means from it, with the 95% confirmation interval $\pm[F_{0.05;1,14}\, V_e\, (1/n_{eff} + 1/r)]^{1/2}$, where V_e is the residual variance, $n_{eff} = 27/(1 + 12)$ and $r = 1$ confirmation run. Because the residual of this deterministic design represents interactions and unassigned columns rather than random error (Section 2.8), the interval indicates the scatter that the additive model leaves unexplained and is not used as a significance test.

3. Results and discussion

This section discusses the optimization process based on CFD simulations, which balances the infection risk of all occupants against draft discomfort in the vehicle cabin while it is being cooled. In addition, this section discusses how the optimization of velocity, temperature, and vent angle can be performed using Taguchi, ANOVA, and GRA methods.

Results obtained from the 27 cases are summarized in Fig. 5. In this experimental design matrix, the response variables are coded as DR and OBJ1-OBJ12. These OBJ variables quantify the Infection Risk probability (IR) for specific source-receptor pathways. OBJ1, OBJ2, and OBJ3 correspond to the IR originating from the Driver to the Front Passenger, Rear Left, and Rear Right occupants, respectively. Similarly, OBJ4 through OBJ6 define the transmission risks from the Front Passenger to the other occupants. The risks originating from the Rear Left passenger are captured in OBJ7 through OBJ9, while OBJ10 through OBJ12 represent the transmission pathways from the Rear Right passenger to the Driver, Front Passenger, and Rear Left occupant, respectively. Transmission pathways coded with the OBJ index are illustrated in Fig. 1. All values are iteration averages with duct-informed inlet profiles (Section 2); the values of all responses, including the worst-seat DR, are listed with those of the nine out-of-array runs of Section 3.6 in Table S1, and the S/N ratios of all responses at each factor level in Table S7.

3.1. Thermal comfort

After solving the 27 scenarios obtained from the L27 orthogonal array shown in Table 2, S/N values were obtained for each objective function. The S/N values calculated using the "smaller is better" approach for the DR, and the contribution ratio (%) values obtained from the ANOVA analysis are shown in Fig. 6. The parameter level corresponding to the highest point of the S/N values obtained for the parameters under consideration indicates the optimum value of that parameter for the objective under investigation. Since the highest value for velocity was obtained at 1 m/s, 1 m/s is considered the optimum level for the velocity parameter. Considering all parameters, the optimal parameter set to minimize DR is: 1 m/s velocity, 20 °C temperature, and a 90 ° orientation angle for all vents. This DR optimum is, however, a warm cabin: at 1 m/s the air temperature at all occupant points lies between 27.1 and 36.4 °C (Table S4), so that DR, which measures draft only, does not penalize the insufficient cooling of the low-velocity cases.

The magnitude of the difference between the lower and upper S/N values of each parameter also directly indicates the importance of that parameter. Fig. 6a shows that, according to the Taguchi method, the most critical parameter for DR is velocity. As the blowing velocity increases, the DR value increases sharply. The second most important parameter is temperature. As seen in Eq. 7, the DR equation includes the

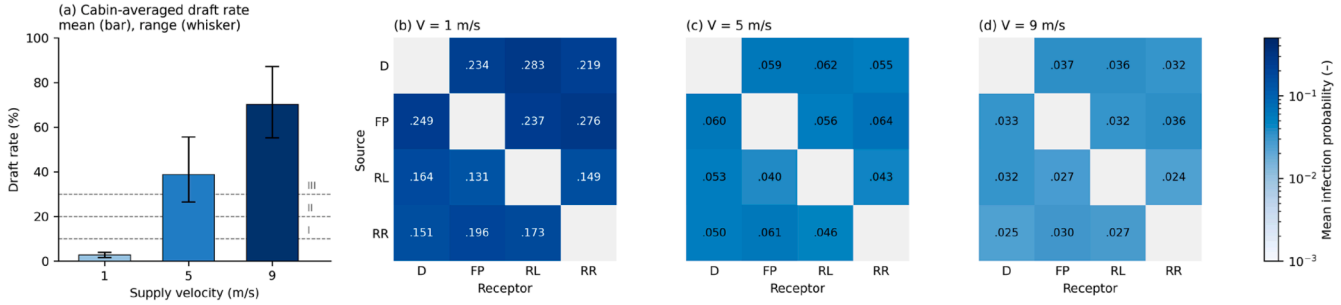

Fig. 5. Summary of the 27 Taguchi cases: (a) cabin-averaged draft rate per supply velocity (bar: mean; whisker: range of the nine cases; dashed lines: ISO 7730 Category I, II and III limits) and (b-d) mean source-to-receptor infection probability at V = 1, 5 and 9 m/s (rows: source, columns: receptor; D: driver, FP: front passenger, RL: rear left passenger, RR: rear right passenger); iteration averages with duct-informed inlet profiles.

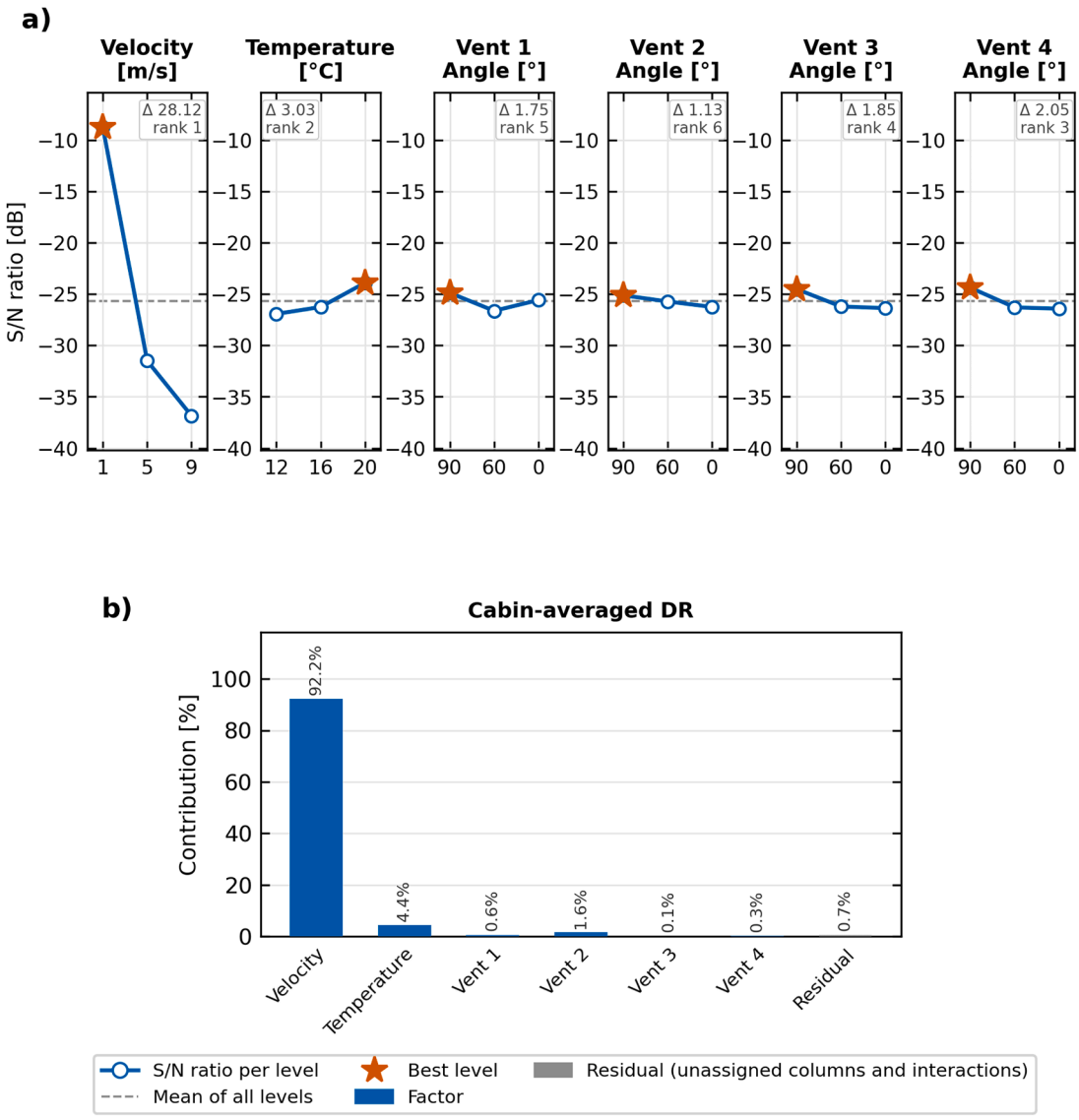

Fig. 6. a) S/N ratios for the cabin-averaged DR, b) contribution ratios obtained from ANOVA for DR.

multiplier (34 - t_a). As the airflow temperature increases, the local temperature on the passenger increases, and the difference between human body temperature and air temperature decreases, thereby reducing the unwanted cooling sensation. This change is therefore consistent with theoretical expectations.

These results are also seen in the ANOVA analysis shown in Fig. 6b and support the Taguchi method results. The ANOVA results reveal that velocity is the major contributor to the cabin-averaged DR, accounting for 92.2%, followed by temperature (4.4%), with blowing angles having a minimal impact on the DR. The sum of the contributions of all angles to ventilation is less than 3%, showing that although blowing angles have a local impact, the overall cabin-averaged thermal comfort due to drafts depends on the jet's momentum and thermal energy rather than its direction. This situation stems from an examination of the average cabin DR value and the strategy considered to ensure the comfort of all four passengers simultaneously.

3.2. Infection risk analysis: driver as a source

Fig. 7a presents the S/N values, and Fig. 7b shows the contribution ratios derived from the ANOVA for the infected driver scenario. This analysis compares the infection probabilities for OBJ1 (Front Passenger), OBJ2 (Rear Left Passenger), and OBJ3 (Rear Right Passenger). According to the "smaller-is-better" concept applied in the Wells-Riley method, the analysis shows that inlet velocity is the most important factor in reducing infection probability. It means that an inlet velocity of 9 m/s gives the maximum value of the S/N ratio. Unlike DR analysis, this result contradicts the requirement for lower velocities for maintaining thermal comfort.

Fig. 7b shows that ANOVA confirms velocity as the dominant factor, contributing 90.1% to 92.7% of the overall variance of the system across all passengers. The higher the velocities, the better the dilution, leading to an increased Air Change Rate (ACH). Consequently, the pathogenic germs are efficiently removed from the vehicle cabin. At 1 and 5 m/s, the Rear Left Passenger (OBJ2), seated behind the driver, receives the highest risk of the three receptors (mean 0.283 and 0.062), whereas at 9 m/s, the three pathways are within 16% of each other (0.032-0.037). Given that the infected air flow is carried backward, the area behind the driver seat is the most significant in terms of infection danger at low and moderate velocities. In turn, OBJ3 (Rear Right Passenger) presents the highest S/N values at all three velocities and hence represents the safest zone.

Regarding the other parameters, the S/N analysis favors 12°C for OBJ1 and OBJ2 and 20°C for OBJ3, but temperature contributes no

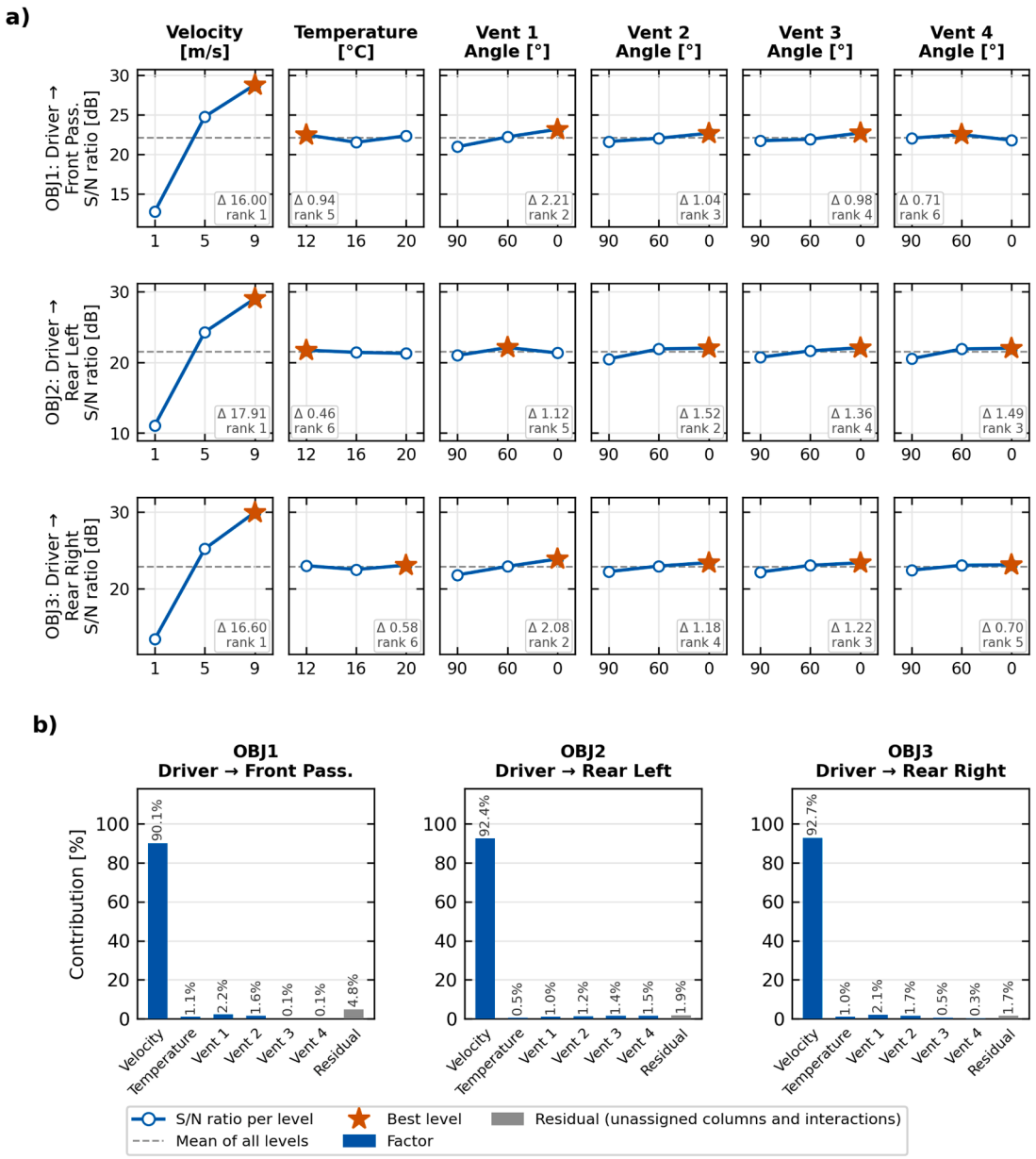

Fig. 7. a) S/N ratios and b) contribution ratios obtained from ANOVA for OBJ1, OBJ2, and OBJ3.

more than 1.1% to the variance. Vent angles show varying optimal values for each occupant; together, the four vent angles account for 4.1-5.2% of the variance, the largest share for the Rear Left Passenger (OBJ2). This outcome is consistent with the flow interaction between the source (driver) and the receptor (Rear Left Passenger) and the turbulent wake structures in this region.

3.3. *Infection risk analysis: front passenger as a source*

The Taguchi analysis of the Front Passenger Infected scenario is based on CFD data and the Signal-to-Noise (S/N) ratio using the L27 orthogonal array in Fig. 8a. Again, the 'smaller-is-better' principle has been adopted to minimize the risk of airborne infection transmission.

The ANOVA contribution ratio results are shown in Fig. 8b. The inlet velocity is the dominant factor in the removal of the contaminants, which accounts for 95.6% of the contribution ratio of the Driver (OBJ4), 95.1% of the contribution ratio of the Rear Left Passenger (OBJ5), and 90.5% of the contribution ratio of the Rear Right Passenger (OBJ6).

The infection risk data shows a clear blocking effect for the Rear Right Passenger (OBJ6), who is sitting directly behind the source. In Case 1, where the velocity is 1 m/s, the infection probability of OBJ6 has a peak of 0.430, which is substantially higher than those of the Driver (0.216) and the Rear Left Passenger (0.253). This is because the two central console vents act as an air curtain, and the front seat blockage causes vortices behind it, which trap the contaminants on the right side of the vehicle.

However, as the flow accelerates, the blocking effect is reduced. In Case 19, where the velocity is 9 m/s, the infection probability for OBJ6 decreases to 0.040, a 91% reduction. The infection risk data shows the high air change rates required to penetrate this seating position's wake zone and break up the vortices.

This research also points out the threat of infection for the Driver (OBJ4), as a result of spillovers sideways. In a slow-flow regime, as in Case 7, the probability of infection for the Driver reaches 0.296, higher than that for the Rear Left Passenger (0.271). This means that, in a slow-flow regime, there is a greater tendency for the contaminant plume to slide sideways across the console and enter the driver's breathing zone. When a fast-flow regime is established, as in cases 19-27, the inertia of

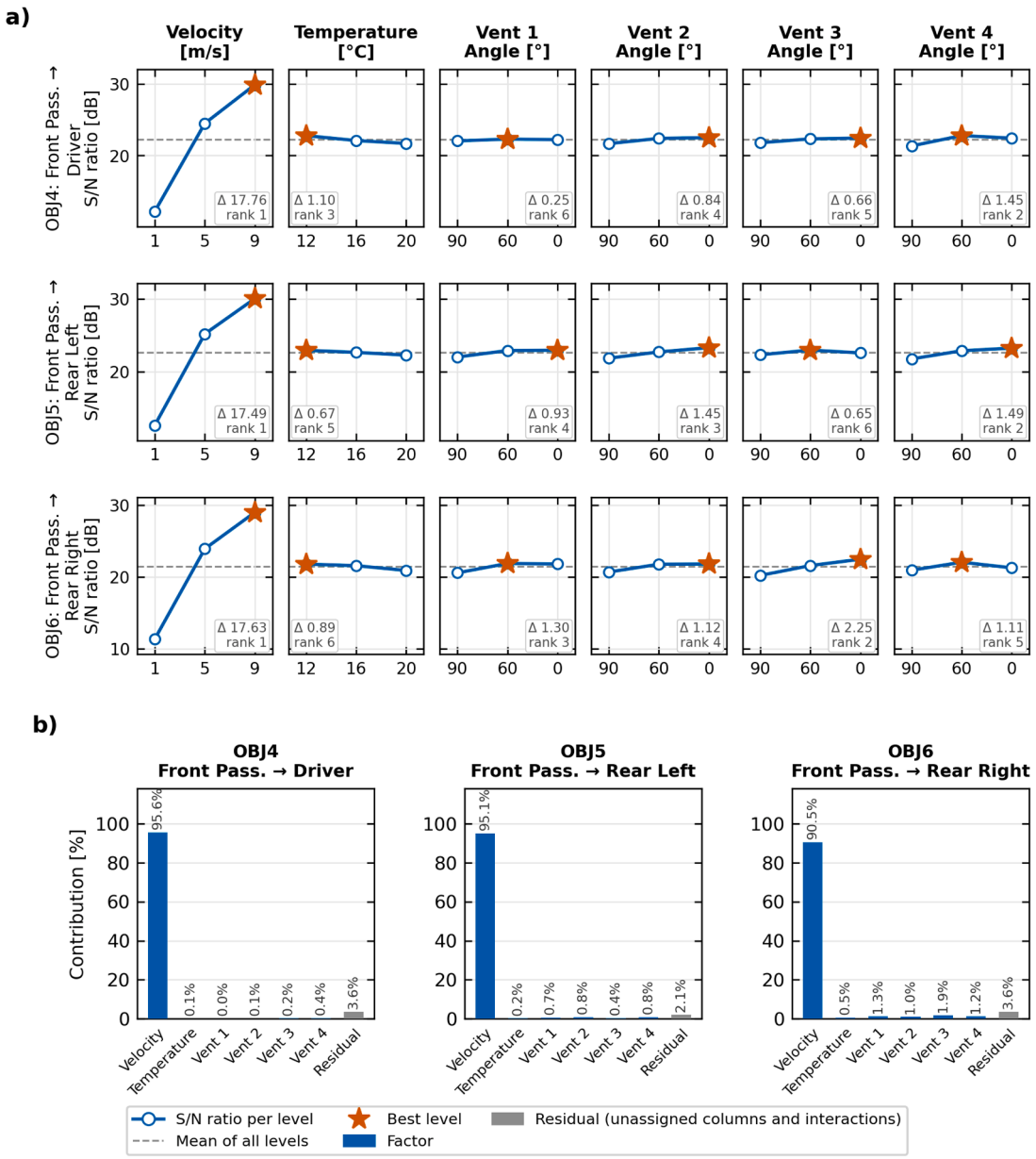

Fig. 8. a) S/N ratios and b) contribution ratios obtained from ANOVA for OBJ4, OBJ5, and OBJ6.

the jet takes over, controlling sideways spread and driving the plume towards the rear exhausts.

Overall, even though the Rear Left Passenger (OBJ5) enjoys geometric isolation due to their diagonal seating arrangement, they remain highly susceptible to dilution of the space (95.1%). To reduce the risk of infection for the Driver and the Rear Right Passenger, a strong, high-velocity airflow is necessary.

3.4. Infection risk analysis: rear left passenger as a source

In the Taguchi optimization problem under consideration, the Rear Left Passenger as the infection source results in a visibly different flow behavior. Fig. 9a shows the S/N ratios for the transmission risks to the Driver (OBJ7), Front Passenger (OBJ8), and Rear Right Passenger (OBJ9). Fig. 9b shows the percentage contributions based on the ANOVA calculations.

While the driver-focused scenario is dominated by the inertial force effect, the spread from the rear passenger to the people in the front row is influenced by other factors as well. The effect of the velocity of the inlet air is considerable in reducing the risk of infection but is less dominant compared to the driver-focused scenario. The percentage contributions based on the ANOVA calculations show that the velocity of the air contributes only 59.0% to the risk to the Driver (OBJ7) and 59.4% to the risk to the Front Passenger (OBJ8). These values are much lower than the more than 90% dominance of the velocity effect when the infection source is in the front row. The reduced role of the inertial force effect in the spread from the rear passenger to the people in the front row indicates that the transport is governed not only by the rate of the air flow but also by the direction of the supply jets and the recirculation zones they create.

The vent angles, in particular those of the side vents, emerge as the second group of factors. Vent 4, the passenger-side vent, contributes 8.4%, 11.2% and 7.2% of the variance of OBJ7, OBJ8 and OBJ9, and Vent 1 and Vent 3 contribute 2.0-5.4% each, while the supply temperature contributes 1.1% or less in the ANOVA. The S/N analysis in Fig. 9a nevertheless favours the lowest temperature (12°C) together with the highest velocity (9 m/s) for all three receptors, with temperature deltas of 3.2-5.8 dB: on the logarithmic scale the small probabilities at 5 and 9

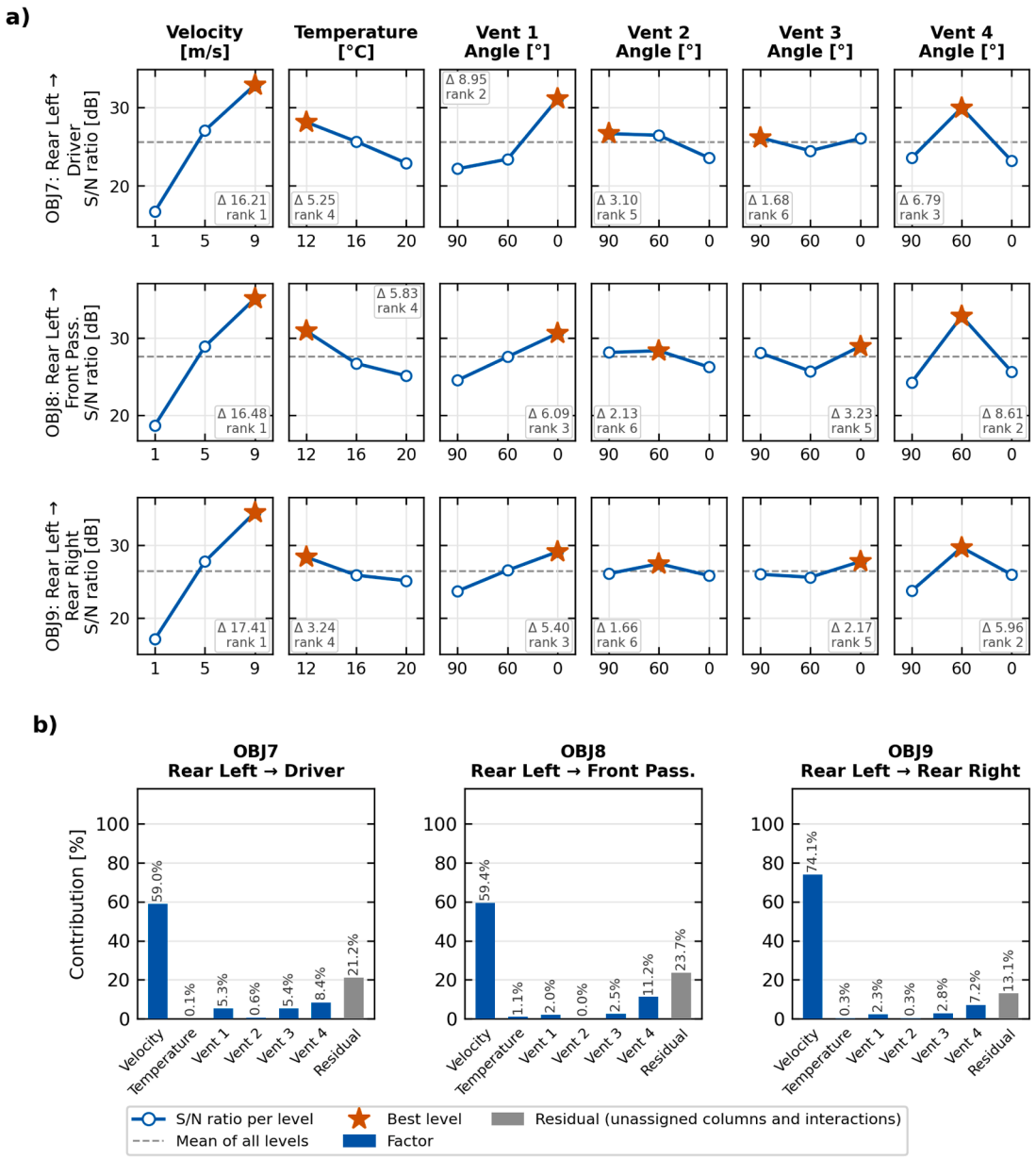

Fig. 9. a) S/N ratios and b) contribution ratios obtained from ANOVA for OBJ7, OBJ8, and OBJ9.

m/s weigh as much as the large ones at 1 m/s, whereas the ANOVA of the response values is dominated by the 1 m/s cases (Section 2.8). A colder supply, i.e. a larger cabin-to-supply temperature difference, thus appears to limit the upstream transport of the rear-left plume at the higher velocities. This effect depends on the thermal field, which was not validated (Section 2.6), and at the optimum vent layout the direct simulations of Section 3.6 show the opposite tendency for these pathways at an unchanged overall infection risk.

For the Rear Right Passenger (OBJ9), who is closest to the source of infection, the velocity contribution is higher at 74.1% compared to the front-row receptors. The infection flow spreading towards the rear of the cabin is influenced by the ventilation flow. Again, the ANOVA analysis shows large residual contributions for the Driver (21.2%) and the Front Passenger (23.7%). In a deterministic design the residual collects the unassigned columns and the interactions between the factors (Section 2.8); its size shows that the transport from the rear-left seat to the front row depends on combinations of velocity and vent angles that the main effects alone do not describe. In other words, even with the increased rate of air change, the geometric isolation of the rear section of the cabin creates a mixed flow regime of convection and diffusion, making it difficult to control the airflow. In order to prevent infection spread from the rear section of the cabin, high-velocity airflow with appropriately directed side vents is necessary to prevent the infection flow from spreading forward.

3.5. *Infection risk analysis: rear right passenger as a source*

In the case of the Rear Right Passenger being identified as the source of infection, the results will be represented as S/N ratios, as depicted in Fig. 10a, and ANOVA contribution rates, as depicted in Fig. 10b. The key issue of interest in this analysis is how this infection will reach the Driver (OBJ10), Front Passenger (OBJ11), and Rear Left Passenger (OBJ12). The analysis validates velocity as the key parameter, but the modes of transmission behave in a nonlinear and complex manner, especially in the diagonal direction towards the Driver.

For the Driver (OBJ10), seated diagonally relative to the source of infection, velocity was found to be responsible for about 64.3% of the variance in infection risks. Of interest, however, is that Vent 1, the

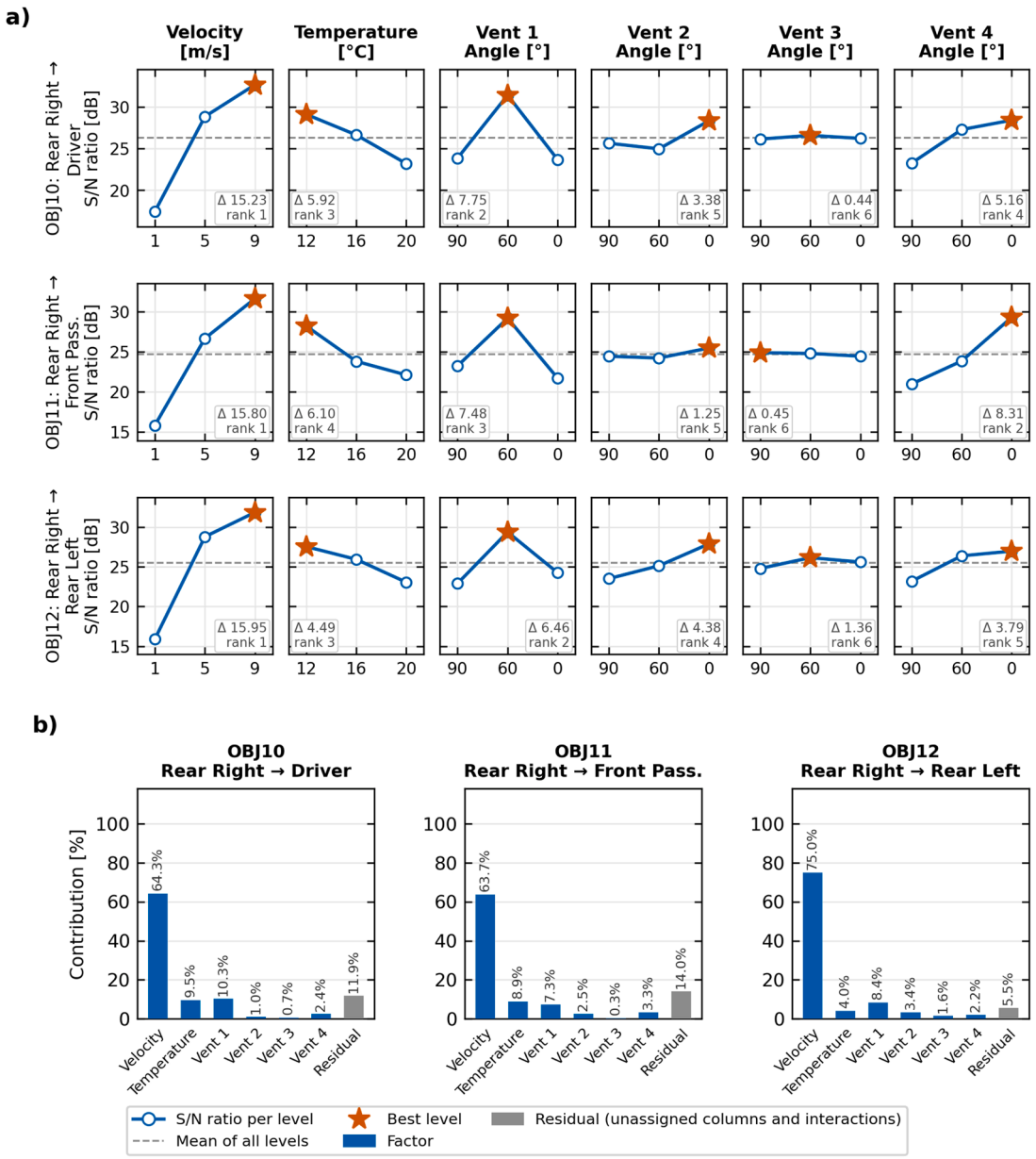

Fig. 10. a) S/N ratios and b) contribution ratios obtained from ANOVA for OBJ10, OBJ11, and OBJ12.

driver-side vent, accounts for 10.3% and the supply temperature for 9.5%, the largest temperature contribution among all pathways, while the residual is 11.9%. Although a higher velocity helps dilute the risk, this transmission path is thus also controlled by the direction of the driver-side jet and by the thermal field. Dead zones behind the front seats can trap impurities, which can later be re-entrained back into the airflow and transported towards the driver's breathing zone by the central reverse airflow.

Unlike direct transmission modes, where impurities move from source to destination along the main flow, along this cross-diagonal path impurities have to pass through the recirculation zones and the wake behind the front seats. The residual of 11.9% for OBJ10 represents the unassigned columns and the interactions between factors rather than random scatter; in particular, the Vent 1 and Vent 2 columns of the array are aliased with the velocity-temperature interaction (Section 2.7), so the L27 alone cannot separate their effects. The direct simulations at 9 m/s in Section 3.6 resolve this point: changing Vent 1 from 60° to 0° or 90° increases the probability of this pathway by a factor of 37-38, which confirms that the driver-side vent controls it.

For the Front Passenger (OBJ11), who is located right in front of the source, the behavior of the aerosol is influenced by the balance between the forward-moving warm plume and the backward-moving ventilation jet. The ANOVA table shows that velocity accounts for about 63.7% of the variance in virus spread, while temperature accounts for about 8.9%. The influence of temperature indicates a role of buoyancy in the forward and upward transport of the aerosol: the S/N analysis prefers the lowest supply temperature (12°C), i.e. a denser, colder supply appears to keep the plume of the infected person from rising towards the person in front. In addition, the influence of the angles of Vent 1 and Vent 2 is about 9.7%; together with OBJ10 and OBJ12 (11.2% and 11.8%), this is higher than for any other source. For OBJ11, Vent 4 has the second-largest S/N range (8.3 dB) but contributes only 3.3% in the ANOVA, which is dominated by the 1 m/s cases.

For the Rear Left Passenger (OBJ12), the virus spread is more lateral. The influence of velocity on the virus's spread is about 75.0%, indicating that the best way to protect an adjacent passenger is to remove the virus quickly by increasing the air exchange rate. The vent angles (Vent 1 8.4%, Vent 2 3.4%) and the temperature (4.0%) play a secondary role,

and the residual is 5.5%. The S/N analysis supports the above finding, as the highest S/N ratio is observed at the highest velocity (9 m/s) and the lowest temperature (12°C) for all three receptors of this source, indicating the lowest infection risk in this case. However, the difference in the explainability of the adjacent risk (OBJ12, residual 5.5%) and the diagonal risk (OBJ10, residual 11.9%) reveals the heterogeneity of the airflow in the cabin and the difficulty of protecting the passengers from a source located behind.

3.6. Multi-objective optimization results

The goal in the multi-objective optimization is to simultaneously optimize 13 performance indicators, including the DR related to thermal comfort and the other 12 related to different Infection Risk probabilities. It is a multidimensional problem that requires a robust decision-support system. For this, the Grey Relational Analysis (GRA) was employed, which reduces the multi-criteria optimization problem to a single overall performance indicator, referred to as the GRG. The GRG values are illustrated in Fig. 11a and tabulated, with the normalized values, grey relational coefficients, weights and S/N ratios, in Table S6; they range from 0.425 (Case 3) to 0.901 (Case 27). Then, the ANOVA method was employed on the GRG values and ranked the control parameters, as shown in Fig. 11c. Inlet velocity emerges as the major parameter, accounting for 90.3% of the total sum of squares, followed by Vent 4 (2.5%), Vent 1 (2.1%) and temperature (1.6%), with a residual of 3.4%. This result confirms that ventilation dilution, driven by the high ACH, is the dominant factor, outweighing the secondary effects of jet direction and thermal management.

Using the GRG metrics as a guide, the best configuration is identified by applying the Taguchi method to these results, with the larger-the-better S/N ratio (Fig. 11b). The mean GRG and its S/N ratio select the same optimum: velocity at level 3 (9 m/s), temperature at level 1 (12 °C), Vent 2 (driver-side center) at 0° (level 3), and Vent 1, Vent 3 and Vent 4 at 60° (level 2), i.e. V3-T1-A12-A23-A32-A42, a combination that lies outside the 27 cases of the array. The margins are small for Vent 3, whose level means at 60° and 0° differ by only 0.0004, and for Vent 2 (0.007 between 0° and 60°); a Monte Carlo propagation of the standard errors of the 13 responses (2000 draws) returns the same mean-GRG optimum in every draw except for Vent 3, which is set to 60° in 65% and to 0° in 35% of the draws, whereas the S/N optimum is returned in 75% of the draws and Vent 2 is set to 60° in most of the others, a setting that the direct simulations C2 and C3 below resolve in favour of 0°. The

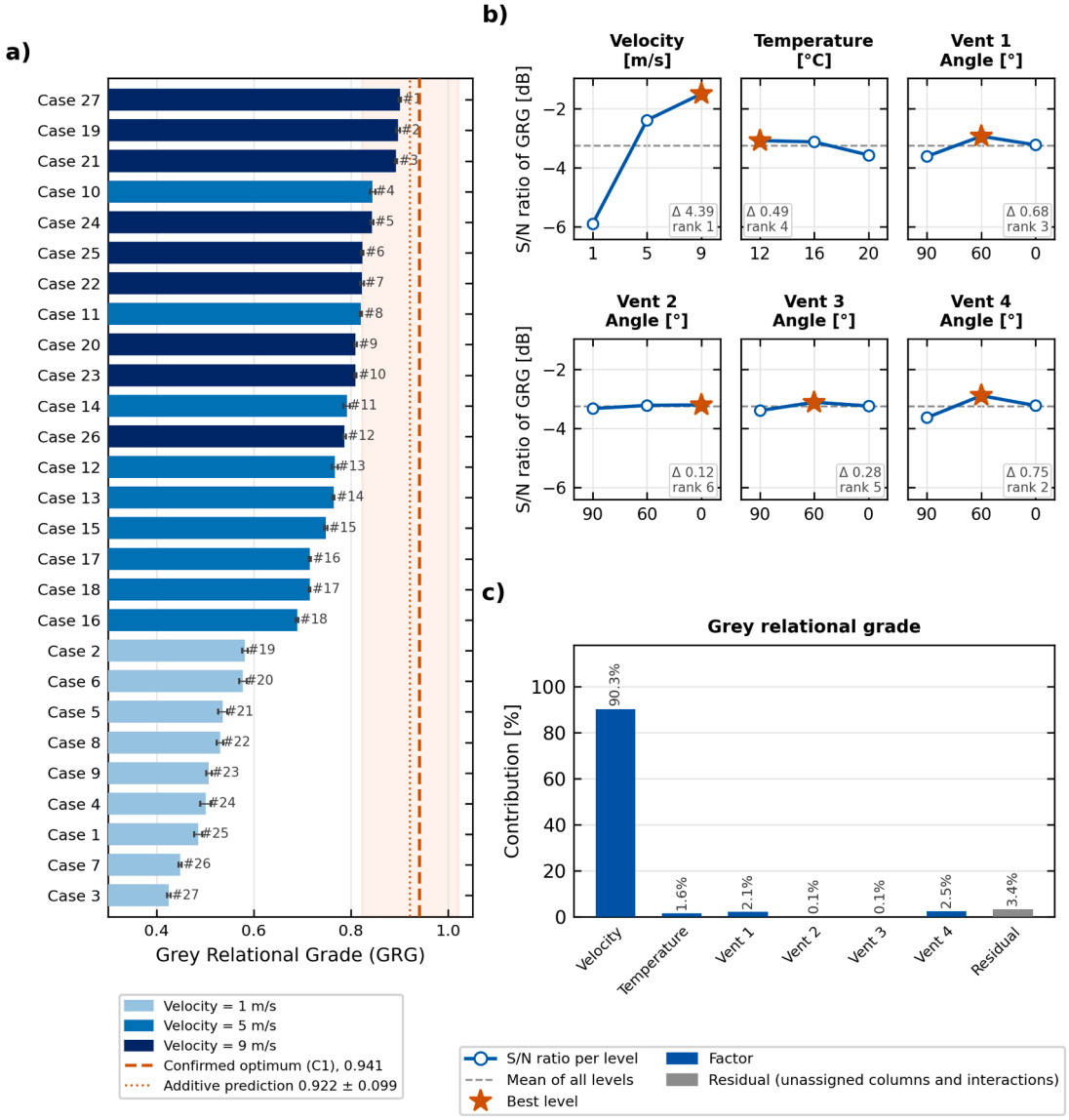

Fig. 11. a) Grey relational grade of the 27 cases (ranked; error bars ±2 standard errors), with the confirmed optimum C1 and its additive prediction (95% interval shaded); b) S/N ratios (larger-the-better) of the GRG for the six factors; c) contribution ratios obtained from ANOVA for the 27 GRG values.

additive prediction for the optimum is GRG = 0.922 ± 0.099 (95% confirmation interval), against 0.901 for the best case of the array (Case 27).

To validate the predicted optimum, it was simulated directly (run C1; Tables 3 and 4). The confirmation run gives GRG = 0.941 ± 0.002, within the 95% interval of the prediction and higher than every case of the array, so the optimum is confirmed. The same vent layout at 16 °C (C8) gives 0.943 ± 0.002, which does not differ from C1 beyond the statistical uncertainty of the iteration averages (+0.002 ± 0.002).

Because the Vent 1 and Vent 2 columns of the array are aliased with the velocity-temperature interaction (Section 2.7), their effects were separated by direct simulations at the optimum velocity and temperature (9 m/s, 12 °C), with the other vents at their optimal angles (Table 4 and Fig. 12). Changing Vent 2 from 0° to 90° (C2) or 60° (C3) lowers the GRG by 0.025 ± 0.003 and 0.090 ± 0.002, and changing Vent 1 from 60° to 0° (C4) or 90° (C5) lowers it by 0.063 ± 0.002 and 0.118 ± 0.002. The optimal angles are thus confirmed at fixed velocity and temperature, and the vent effects at this operating point are 2.7-13 times (Vent 2) and 2.3-3.4 times (Vent 1) larger than the main effects of the array, which average over all velocities; for Vent 2 the order of the 60° and 90° settings is even reversed. A 2 × 2 set of runs with Vent 2 at 0° and 90° and the supply at 12 and 20 °C (C1, C2, C6, C7) shows that the Vent 2 effect does not depend on the supply temperature (−0.025 ± 0.003 at 12 °C and −0.029 ± 0.002 at 20 °C; interaction −0.003 ± 0.003). Vent 3 and Vent 4 were not varied at the optimum layout, so their settings rest on the array: the Vent 3 contribution to the GRG is 0.1% and its level means differ by 0.0004, and the only direct comparison, C7 against C9 at 20 °C with Vent 2 at 90°, favors Vent 3 at 90° (GRG 0.917 and 0.933). The Vent 3 setting is therefore not resolved by the present runs.

At the optimum vent layout the supply temperature has little effect on the GRG: 0.941 at 12 °C (C1), 0.943 at 16 °C (C8) and 0.946 at 20 °C (C6). The gain from 12 to 20 °C (+0.005 ± 0.002) comes from the DR term, whereas the infection term does not change (+0.000 ± 0.002): the mean infection probability of the twelve pathways is 1.47% at 12 °C and 1.51% at 20 °C (+2.8%, 1.3 standard errors), the rear-left-source pathways decreasing and the front-passenger-to-driver pathway increasing. The cabin-averaged DR falls from 82.8% at 12 °C to 76.2% at 16 °C and 67.7% at 20 °C. The main effect of the array, which favours 12 °C, therefore does not hold at this operating point (an interaction with velocity, with which the temperature main effect is aliased; Section 2.7), and the additive model under-predicts all three runs at 20 °C (C6, C7, C9) by 0.050-0.077. In practice the supply temperature can be chosen for comfort at the optimum vent layout: C6 has the highest GRG of all 36 simulations, followed by C8 and C1, so the three highest grades all belong to this vent layout. C6 is therefore the recommended operating point of this vent layout, whereas C1 is the optimum predicted by the main-effect model.

The direct runs also show where the optimum vent layout gains its advantage. In each of the four single-vent deviations at 12 °C (C2-C5), 66-88% of the loss in the infection term of the GRG arises from the rear-source pathways (OBJ7-OBJ12), and the three pathways whose probability increases most are those from the rear-right occupant (by factors of 5-38). Fig. 13 compares the rear-right source in C1, C5 and C3: in the optimum the tracer remains behind the rear-right occupant and is carried to the exhaust, and its probability in the front half of the cabin is of the order of 10^{-3}; with Vent 1 at 90° (C5) the tracer is carried forward along the roof and the probability rises to about 10^{-2} throughout the cabin; with Vent 2 at 60° (C3) a forward-moving band along the roof remains. Because the velocity magnitude is prescribed, a vent at 90° also supplies about 44% less air than at 60° (Table S2), so the C5 deviation combines a change of direction with an 11% lower total supply; C4, whose supply is almost unchanged, shows that the direction alone already lowers the GRG by 0.063. Table 3 compares the optimum with the best and worst cases of the array. Relative to the worst case (Case 3), the optimum reduces the mean infection probability by 94.4%, and the individual pathways by 87.5-99.7%. Relative to the best case of the array (Case 27, also at 9 m/s), it lowers the mean infection probability by 31% (from 2.14% to 1.47%), through 52-94% lower probabilities on the rear-source pathways, whereas the front-source pathways change by only 3-18% and the highest single pathway (front passenger to rear right, 3.39% and 3.30%) is nearly unchanged; the price is a higher cabin-averaged DR (82.8% against 64.8%).

The DR in the optimum condition is far above the ISO 7730 categories: the cabin average is 82.8% and the worst seat 99.3% (Table 3), against the Category III limit of 30%. The high DR is inherent to the 9 m/s supply that dilutes the pathogens effectively: all nine cases of the array at 9 m/s exceed Category III (cabin average 55.2-87.1%, worst seat 72.1-98.7%), and the local air speeds at the occupants reach about 2 m/s (Table 5; the local DR of all cases is shown in Fig. S1), well outside the validity range of Eq. 7, so that these values indicate a strong draft rather than a calibrated percentage of dissatisfied. Raising the supply temperature to 20 °C at the optimum vent layout (C6) lowers the cabin-averaged DR to 67.7% and the worst seat to 93.0% at an unchanged infection risk; at this velocity a lower DR is obtained only with vent layouts that raise the infection risk (Cases 25-27, C7 and C9; Table 4 and Table S1). Among these, C9 gives the lowest worst-seat DR of all runs at 9 m/s (71.0%) at a mean infection probability of 1.84%. At 5 m/s, within the measured capacity of passenger-car HVAC units, the best configuration is Case 10 (5 m/s, 12 °C, vents 60°/0°/90°/60°), which shares the optimal angles of Vent 1, Vent 2 and Vent 4 and reaches GRG 0.844 with a cabin-averaged DR of 50.2% and a mean infection probability of 3.6%. At these supply rates comfort and infection control are opposing objectives: the optimum, like every configuration with a low infection risk, is a temporary high-dilution mode for periods of elevated infection risk, not a comfortable operating point.

The GRA weights the DR by 9.3%, partly because there are twelve infection objectives and partly because they respond more strongly to the factors (Section 2.9). When the DR weight is raised and the infection weights are scaled down proportionally, the optimum of the mean GRG

Table 3
Quantitative comparison of the confirmed optimum (C1, 12 °C), the optimum vent layout at 20 °C (C6), the best L27 case (Case 27), and the worst L27 case (Case 3); GRG, cabin-averaged and worst-seat draft rate (DR, DR_{ws}, %) and infection probability of the twelve pathways.

Parameter	C1: optimum, 12 °C	C6: optimum layout, 20 °C	Case 27 (best L27)	Case 3 (worst L27)
GRG	0.941	0.946	0.901	0.425
DR (%)	82.8	67.7	64.8	3.1
DR_{ws} (%)	99.3	93.0	79.2	4.5
OBJ1 (D → FP)	0.0291	0.0312	0.0328	0.3298
OBJ2 (D → RL)	0.0300	0.0311	0.0335	0.2840
OBJ3 (D → RR)	0.0243	0.0259	0.0296	0.2666
OBJ4 (FP → D)	0.0198	0.0243	0.0222	0.3024
OBJ5 (FP → RL)	0.0228	0.0237	0.0279	0.2821
OBJ6 (FP → RR)	0.0330	0.0341	0.0339	0.2637
OBJ7 (RL → D)	0.0066	0.0032	0.0207	0.3264
OBJ8 (RL → FP)	0.0033	0.0017	0.0069	0.2637
OBJ9 (RL → RR)	0.0037	0.0020	0.0077	0.2169
OBJ10 (RR → D)	0.0007	0.0009	0.0110	0.2133
OBJ11 (RR → FP)	0.0023	0.0024	0.0175	0.1658
OBJ12 (RR → RL)	0.0009	0.0010	0.0129	0.2573
Mean IR	0.0147	0.0151	0.0214	0.2643
Max IR	0.0330	0.0341	0.0339	0.3298

Table 4
Out-of-array simulations at 9 m/s: confirmation run (C1), decoupling runs for Vent 2 (C2, C3), Vent 1 (C4, C5) and Vent 2 × temperature (C6, C7), and two further configurations (C8: the optimum vent layout at 16 °C; C9: 20 °C with Vent 2 and Vent 3 at 90°); GRG ± standard error, additive prediction and difference, DR (%) and mean and maximum infection probability of the twelve pathways (%).

Run	T (°C)	Vents 1/2/3/4 (°)	GRG ± SE	Predicted	CFD − pred.	DR	DR_{ws}	Mean IR	Max IR
C1	12	60/0/60/60	0.941 ± 0.002	0.922	+0.019	82.8	99.3	1.47	3.30
C2	12	60/90/60/60	0.916 ± 0.002	0.912	+0.003	81.7	97.5	1.92	4.40
C3	12	60/60/60/60	0.852 ± 0.002	0.915	−0.064	80.9	96.9	2.87	4.86
C4	12	0/0/60/60	0.878 ± 0.001	0.903	−0.025	85.9	96.4	2.34	3.39
C5	12	90/0/60/60	0.823 ± 0.001	0.870	−0.046	78.2	96.6	3.35	6.53
C6	20	60/0/60/60	0.946 ± 0.001	0.877	+0.069	67.7	93.0	1.51	3.41
C7	20	60/90/60/60	0.917 ± 0.001	0.867	+0.050	65.7	89.0	1.97	4.37
C8	16	60/0/60/60	0.943 ± 0.002	0.908	+0.036	76.2	98.9	1.49	3.33
C9	20	60/90/90/60	0.933 ± 0.001	0.856	+0.077	59.4	71.0	1.84	4.73

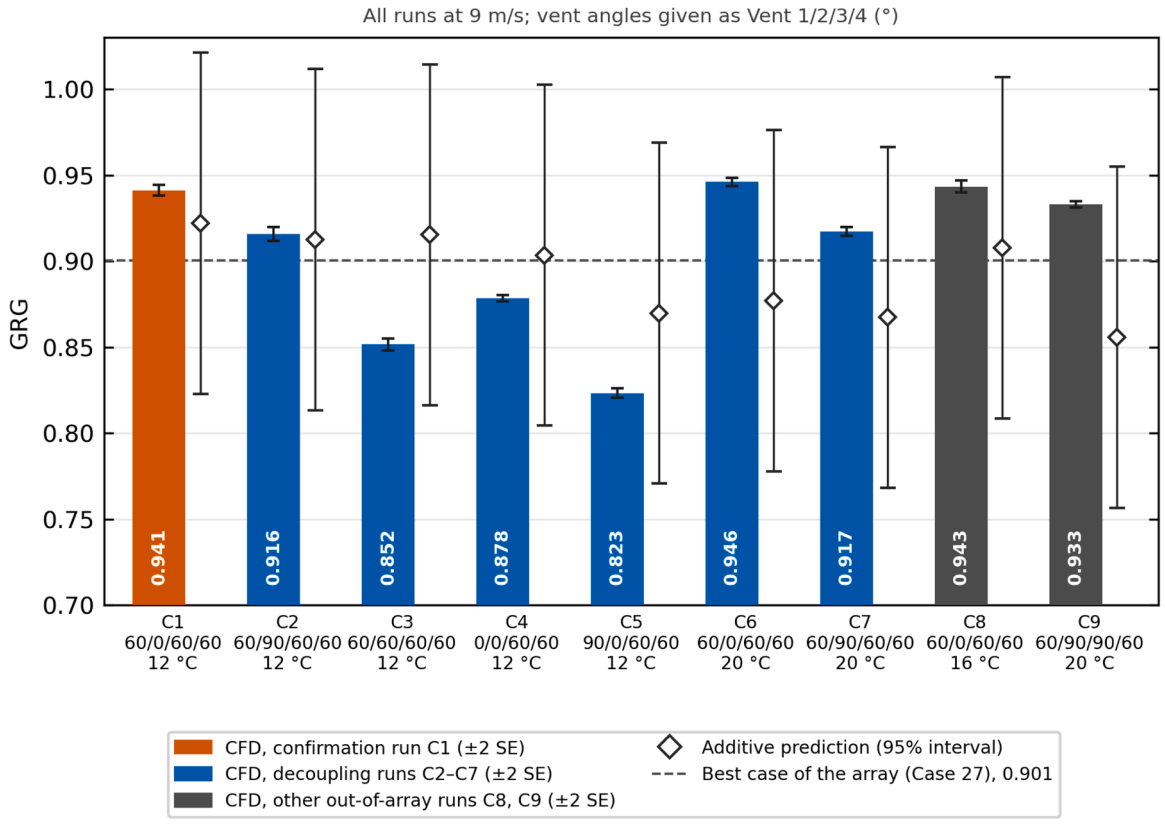

Fig. 12. Grey relational grade of the confirmation run (C1), the decoupling runs (C2-C7) and the further out-of-array runs (C8, C9), all at 9 m/s, with the additive predictions (95% interval) and the best case of the array; error bars ±2 standard errors.

remains unchanged for DR weights below 0.23 and that of the S/N ratio below 0.16, both then setting Vent 2 to 60°; the optimum retains 9 m/s up to a DR weight of 0.40 (with a supply at 16 °C from 0.375 for the mean GRG and from 0.34 for the S/N ratio) and moves to 5 m/s at 0.405 and to 1 m/s at 0.43 (Table S8). Replacing the cabin-averaged DR by the worst-seat DR leaves the S/N optimum unchanged, the mean-GRG optimum then setting Vent 3 to 0° instead of 60° (a difference of 0.003 in the level means), and preserves the GRG ranking of the 27 cases (Spearman $\rho = 0.995$). The absolute probabilities depend on the quanta emission rate. The value used here, $q = 20$ quanta/h, lies between the activity-matched values for seated occupants of 3.1 (resting) and 42 quanta/h (light activity, speaking) [46,47]. Over this range the mean pathway probability of the optimum varies from 0.23% to 3.05% and its reduction relative to the worst case from 95.1% to 93.5%, and the S/N analysis returns the same optimum (the mean GRG at 42 quanta/h preferring Vent 3 at 0°). Computing OBJ from the sphere-averaged quanta concentration instead of averaging P_{local} leaves the optimum unchanged, whereas using the maximum of P_{local} in the sphere favours Vent 2 at 60° and Vent 3 at 0° (and, for the S/N ratio, 16 °C; Table S8); the volume average is retained because the receptor inhales from the whole breathing zone rather than from its most exposed point.

The additive model of the Taguchi analysis was checked against all nine out-of-array runs (Table 4): the differences between simulation and prediction range from −0.064 to +0.077 (RMS 0.049) and all lie within the 95% interval of ±0.099, but the predictions span only 0.066 and their rank correlation with the simulated grades is zero. The additive model is therefore adequate for locating the optimum region but cannot rank configurations as close as the present ones; for this reason the optimal vent angles are based on the direct simulations rather than on the prediction alone.

Fig. 14 shows the local infection probability fields of the confirmed optimum (C1) for each of the four sources, in a vertical plane through the source and in the horizontal plane at breathing height. For the front-row sources (Fig. 14a and 14b) the high-momentum supply sweeps the

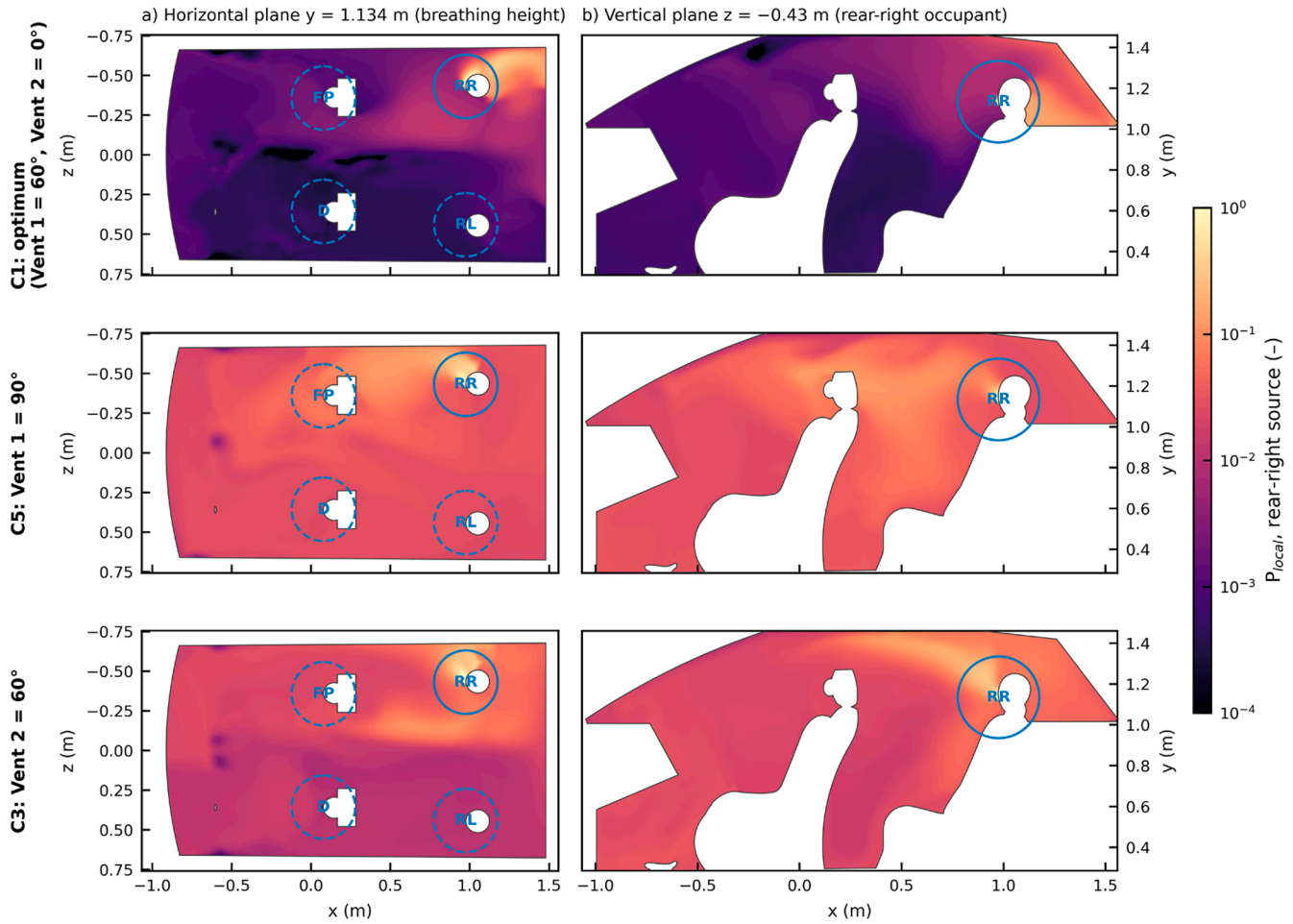

Fig. 13. Local infection probability of the rear-right source in the optimum (C1) and with Vent 1 at 90° (C5) or Vent 2 at 60° (C3): a) horizontal plane at breathing height, b) vertical plane through the rear-right occupant; circles mark the 0.4 m spheres (fields of the final iteration).

Table 5
Local air temperature T (°C), mean speed V (m/s) and DR (%) at the three heights of each occupant (0.10, 0.60 and 1.10 m) in the optimum (C1, 12 °C) and with the same vent layout at 20 °C (C6).

Occupant	Height (m)	C1: T	C1: V	C1: DR	C6: T	C6: V	C6: DR
Driver	1.1	19.8	0.78	99.6	25.2	0.59	69.9
	0.6	22.0	0.37	48.7	26.7	0.33	26.9
	0.1	22.1	0.51	44.8	26.6	0.50	29.6
	Seat mean			64.4			42.2
Front passenger	1.1	20.0	0.70	96.1	25.4	0.70	71.8
	0.6	20.1	0.87	97.3	26.1	0.69	67.6
	0.1	22.7	0.30	30.6	27.2	0.48	24.6
	Seat mean			74.7			54.7
Rear left	1.1	19.8	0.73	100.0	25.2	0.68	99.3
	0.6	18.8	2.04	100.0	24.5	1.87	100.0
	0.1	19.7	0.53	93.4	25.0	0.65	79.7
	Seat mean			97.8			93.0
Rear right	1.1	19.5	0.61	100.0	25.3	0.62	80.0
	0.6	18.7	1.96	100.0	24.5	2.06	100.0
	0.1	20.0	0.77	97.9	25.1	0.61	68.7
	Seat mean			99.3			82.9

tracer rearwards, and the probability in the rear breathing zones is of the order of 10^{-2}; for the rear sources (Fig. 14c and d) the tracer is confined to the rear of the cabin and carried to the exhaust, and the probability in the front breathing zones is of the order of 10^{-3}. The contour plots thus show how the optimized ventilation strategy limits the region of elevated infection probability to the vicinity of the source and the exhaust paths. The fields are those of the final iteration, whereas the OBJ values are iteration averages.

3.7. *Effect of the duct-informed inlet*

To assess the effect of the inlet treatment, the duct-informed results were compared with uniform-inlet solutions of the same 27 cases, obtained with the same mesh, models and flow rates (Fig. S2). At equal flow rates the duct-informed profiles carry 21-67% more momentum and more turbulence than a uniform inlet (Section 2.2.1). The cabin-averaged DR is higher by a median of 8% at 1 m/s, 16% at 5 m/s and 13% at 9 m/s (relative changes), and the infection probabilities change by a median factor of 0.97-1.05 for the front-source pathways and 1.07-1.24 for the rear-source pathways. The ranking of the 27 cases is largely preserved: Spearman $\rho = 0.995$ for the DR, 0.963 for the mean infection probability and 0.946 for the GRG; for the individual pathways $\rho = 0.95$-0.97 for the front sources but 0.78-0.93 for the rear sources, whose transport depends most on the jet structure. Part of these differences arises because the uniform-inlet values are single-iteration results, whereas the duct-informed values are iteration averages (Section 2). Since single-iteration probabilities can differ from their averages by factors of 0.43 to 1.40 (Section 2), the comparison resolves the changes in DR and GRG but not the 0.10 percentage point difference in mean

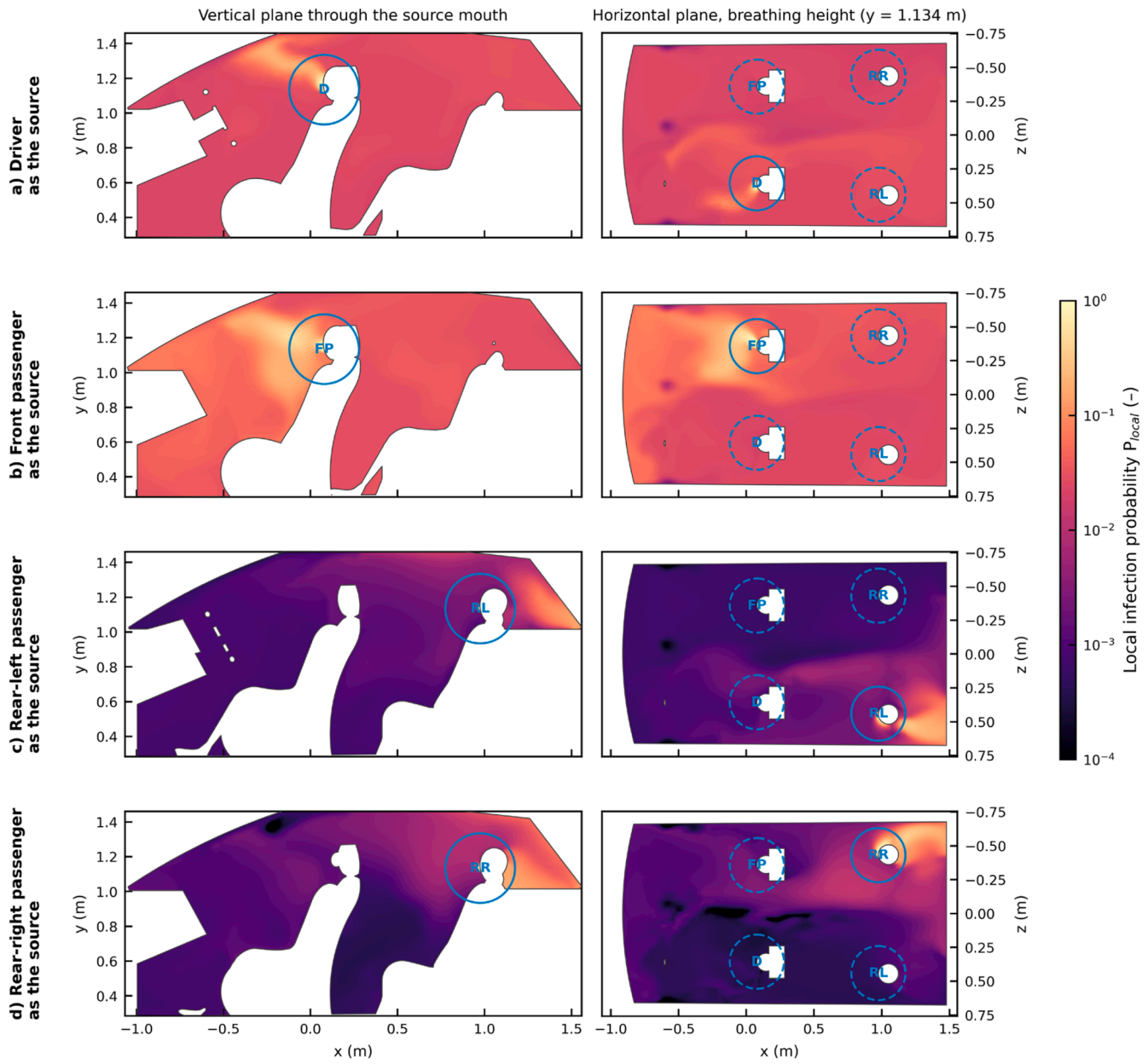

Fig. 14. Local infection probability P_{local} in the confirmed optimum (C1) with a) the driver, b) the front passenger, c) the rear-left passenger and d) the rear-right passenger as the source: vertical plane through the source mouth (left) and horizontal plane at breathing height (right); circles mark the 0.4 m spheres, the solid circle that of the source (field of the final iteration).

infection probability between C8 and Case 27 with the uniform inlet.

Table 6 compares two configurations in detail, the optimum vent layout at 16 °C (C8) and the best case of the array (Case 27). With the duct-informed inlet, the cabin-averaged DR of both configurations increases by 7-8 percentage points, and the mean infection probability decreases for C8 (from 1.65% to 1.49%) and increases for Case 27 (from 1.75% to 2.14%). With either inlet Case 27 has the lower DR and C8 the lower mean infection probability, with the uniform inlet by a small margin (1.65% against 1.75%, single-iteration values). Their GRGs are practically equal with the uniform inlet (0.926 and 0.925, single-iteration values) and clearly separated with the duct-informed inlet (0.943 against 0.901). With the uniform inlet, the mean GRG is highest for 9 m/s, 12 °C and vents 60°/0°/90°/60°, which differs from the duct-informed optimum only in Vent 3, whose contribution to the GRG is 0.1% (Table S5), whereas the S/N ratio of the GRG prefers Vent 2 at 90° (Table S8); the Vent 2 setting, which the array cannot separate from the velocity-temperature interaction, was therefore fixed by the direct runs of Section 3.6. The side vents at 60° are obtained with both inlet

Table 6
Uniform versus duct-informed inlet for the optimum vent layout at 16 °C (C8) and the best case of the array (Case 27); the uniform-inlet values are single-iteration results.

Configuration	Inlet	DR (%)	Mean IR (%)	Max IR (%)	GRG
C8: 9 m/s, 16 °C, 60/0/60/60	uniform	69.0	1.65	3.79	0.926
	duct-informed	76.2	1.49	3.33	0.943
Case 27: 9 m/s, 20 °C, 60/90/0/60	uniform	57.3	1.75	4.32	0.925
	duct-informed	64.8	2.14	3.39	0.901

treatments, and the separation between configurations becomes clearer with the duct-informed inlet.

4. Limitations and future work

The quantitative results, particularly those involving the optimum vent angles, were generated using the assumptions of a general SUV cabin geometry and can thus only be applied to this geometry and not to others, such as sedans, minivans, or public transportation buses. However, while the geometry-dependent optimal values cannot be applied directly to other geometries, the method used, which combined the Taguchi-GRA multi-objective optimization approach with the local Wells-Riley model, is geometry-independent. Thus, an asymmetric, high-momentum vent design approach is applicable and should be adapted according to the new geometry.

The modeling simplifications adopted for computational efficiency define the scope of the present results. Specifically, the steady RANS closure with the standard k-ε model represents the mean flow rather than instantaneous unsteady wake structures. The Eulerian tracer-gas approach models the fine airborne aerosol fraction instead of large-droplet dynamics. Furthermore, the respiratory source is modeled as steady rather than transient. Thermal comfort is evaluated solely using the Draft Rate, and a single ventilation mode with six design factors is considered.

Four limitations are of first order. First, the vent jets are represented by duct-informed profiles from the face-vent ducts of a different vehicle, scaled to the vents of the generic cabin; the vanes are not modelled and the nominal jet direction is imposed, whereas the jet of a real vent can deviate from the direction set by its vanes by more than 10° [55], so the optimal angles are nominal settings that should be re-established for a specific vehicle. The vent angle factors also change the vent flow rate ($\rho VA \cos\theta$), by up to 44% at a vent and up to 23% in total at 9 m/s, so their effects combine jet direction and supply rate. Second, the validation covers the isothermal velocity field only; buoyancy, radiation and solar loading are unvalidated, and the supply-temperature contributions to the rear-source pathways are most exposed to this. Third, the draft-rate correlation was derived for sedentary, near-neutral subjects at low local speeds, and most occupant points lie outside its validity range, so DR is here a relative index of draft risk rather than a calibrated percentage. Fourth, the 9 m/s level, at which the optimum is found, is at or beyond the upper end of the supply rates of passenger-car HVAC units (Section 2.2). On the optimization framework: Taguchi-GRA searches only the discrete level grid, rests on an additive model that cannot rank configurations as close as the present ones (Section 3.6), aliases the main effects of the vents and of the temperature with interactions involving velocity in a six-factor L27 (Section 2.7), resolved here by direct simulations only at 9 m/s around the optimum, and returns one weighted compromise rather than a Pareto front; a Taguchi screening → surrogate → metaheuristic refinement path would recover the Pareto front. Thermal comfort is assessed by DR alone; the equivalent temperature of ISO 14505 captures radiant asymmetry, which DR cannot, but omits turbulence intensity, which DR encodes, so the two are complementary, and computing it would require a calibrated segmented numerical manikin. Finally, the tracer is released as pure N_2O, which is denser than exhaled air close to the mouth (Section 2.1).

These limitations will be addressed in future work. Planned improvements include alternative turbulence closures (SST k-ω) and scale-resolving simulation (Large Eddy Simulation) and an Eulerian-Lagrangian discrete-phase model incorporating droplet evaporation. Time-resolved simulations of transient respiratory events, such as coughing and sneezing, will also be conducted. Additionally, whole-body comfort indices like PMV and PPD will be incorporated, other ventilation modes will be explored, and a dedicated experimental validation will be performed in a real, instrumented vehicle cabin.

The highest-priority extensions are a vehicle-specific duct and vane model to verify the nominal jet directions, a non-isothermal benchmark with simultaneous temperature and tracer measurement, a solar-loaded versus shaded comparison, and a full factorial of the Vent 1 and Vent 2 angles at lower supply velocities, where the vent effects were resolved only through the aliased columns of the array.

5. Conclusion

This research proposed an inclusive multi-objective optimization approach to balance the risk of airborne cross-infection against draft-induced thermal discomfort in the vehicle cabin. The proposed approach used three-dimensional CFD simulations with duct-informed inlet profiles, the local Wells-Riley infection risk model, the Taguchi method with an L27 orthogonal array, analysis of variance, Grey Relational Analysis, and direct confirmation and decoupling simulations, yielding the following key results:

1. The velocity of the inlet air has the strongest effect on all performance parameters. The ANOVA analysis confirms the dominant role of velocity, which explains 92.2% of the variance in the cabin-averaged DR and 59.0% to 95.6% of the variance in infection risk, depending on the particular source-receptor pathway. Because the supply velocity both dilutes the pathogens and generates the draft, it dominates the trade-off between the two objectives.
2. The mode of pathogen transport is strongly dependent on the location of the infection source. When the infection source is placed in the front row (driver or front passenger), the supply air jets have the strongest effect on pathogen removal, with velocity accounting for more than 90% of the variance. When the source is placed in the rear seats, the velocity contribution falls to 59-75%, the side vents (Vent 4 for the rear-left and Vent 1 for the rear-right source) contribute 7-11%, and the supply temperature contributes up to 9.5% (rear-right source to driver). This temperature contribution, and the preference of the S/N analysis for 12°C on the rear-source pathways, depend on the computed thermal field, which was not validated (Section 2.6); at the optimum vent layout a 20°C supply did not change the overall infection risk. The ANOVA residuals for the rear-source pathways, up to 23.7%, represent the unassigned columns and the interactions between the factors, i.e. transport that the main effects alone do not describe.
3. The GRA-based optimization predicted the optimum V = 9 m/s, T = 12°C and nominal vent angles A1 = 60°, A2 = 0°, A3 = 60° and A4 = 60° from the main effects of the array, confirmed by a direct simulation with duct-informed inlet profiles (GRG 0.941 against a predicted 0.922 ± 0.099); at this layout the supply temperature has little effect, and 20°C gives the highest grade of all runs (0.946). Direct simulations at fixed velocity and temperature confirmed Vent 1 at 60° and Vent 2 at 0° independently of the aliasing in the array, without a Vent 2 × temperature interaction; the Vent 3 setting has a negligible effect and is not resolved by the present runs. The asymmetric arrangement, with the driver-side center vent directing its jet horizontally rearwards and the other vents at 60°, suppresses the forward and diagonal transport from the rear seats, which accounts for 66-88% of the losses when Vent 1 or Vent 2 deviates from its optimal angle (C2-C5).
4. The confirmed optimum reduces the mean infection probability for all 12 source-receptor pathways to 1.47%, with no single pathway above 3.30%. Compared with the worst-performing case in the L27 array (Case 3), it reduces the mean infection risk by 94.4%; compared with the best-performing case in the L27 array (Case 27), it lowers the mean infection probability by 31% (1.47% vs. 2.14%), mainly through 52-94% lower probabilities on the rear-source pathways, at a cost in DR (82.8% vs. 64.8%).
5. The optimum results in a cabin-averaged DR of 82.8% and a worst-seat DR of 99.3%, far above ISO 7730 Category III (30%), as do all configurations at 9 m/s; at the optimum vent layout a 20°C supply lowers these values to 67.7% and 93.0% at an unchanged infection

risk, so that the supply temperature can be chosen for comfort. The 9 m/s level is at or beyond the upper end of the supply rates of passenger-car HVAC units. This positions the suggested strategy as a temporary high-dilution mode for periods of increased infection risk, not a comfortable operating point; within the capacity of typical units, the best configuration at 5 m/s (Case 10) shares the optimal angles of Vent 1, Vent 2 and Vent 4.

The results of this study will be useful to both the academic research community and the automotive industry. The suggested methodology, based on a local CFD-coupled Wells-Riley model and Taguchi-GRA multi-objective optimization, is geometry-independent and can be used in any confined transportation space, including sedans, minivans, buses, and trains, provided the vent configurations are re-optimized for the new geometry. It should be noted that the obtained results, in terms of quantified optimal vent angles, correspond to the generic SUV geometry. In addition, the values of the infection risk depend on the values of the quanta generation rate ($q = 20$ quanta/h) and exposure time ($t = 2$ h), and for different pathogens characterized by different rates of emission of infectious quanta and/or different trip durations, the absolute values of the risk will be different.

Future research could explore the dynamics of actions such as sneezing and coughing at different time intervals within the transient regime. Additionally, employing direct droplet modeling would provide valuable insights into deposition mechanics.

Declaration of generative AI And AI-assisted technologies in the manuscript preparation process

During the preparation of this work, the authors used Claude, Gemini and Grammarly to refine the language, improve the readability and check the internal consistency of the manuscript. After using these tools, the authors reviewed and edited the content as needed and take full responsibility for the content of the published article.

CRediT authorship contribution statement

Bahadir Erman Yuce: Writing – review & editing, Writing – original draft, Visualization, Methodology, Investigation, Formal analysis, Data curation, Conceptualization. **Yunus Emre Cetin:** Writing – review & editing, Writing – original draft, Investigation, Conceptualization. **Martin Kriegel:** Writing – review & editing, Conceptualization.

Declaration of competing interest

The authors declare that they have no known competing financial interests or personal relationships that could have appeared to influence the work reported in this paper.

Acknowledgments

Bahadir Erman Yuce acknowledges support from the Research Projects Coordination Office of Bursa Uludağ University (Project No: FGA-2025-2002). The author thanks the BUU BAP Unit for its support.

Supplementary materials

Supplementary material associated with this article can be found, in the online version, at doi:10.1016/j.buildenv.2026.115498.

Data availability

Data will be made available on request.

References

[1] J. Park, S. Park, H.S. Choi, J. Hwang, Air purifier and ventilation fan effects on SARS-CoV-2 airborne transmission in vehicle: infection risk analysis with zonal and CFD models, Process Saf. Env. Prot. 201 (2025) 107619, https://doi.org/10.1016/j.psep.2025.107619.
[2] H. Zhang, T. Wang, Y. Zeng, H. Li, Y. Zhu, F. Shi, Y. Wang, Y. Lu, J. Zhou, Effects of exhalation directions on particle dispersion in high-speed train cabin and seat allocation strategies: an experimental and numerical study, Build. Env. 284 (2025) 113483, https://doi.org/10.1016/j.buildenv.2025.113483.
[3] B.I. Bittelbrunn, H.S. Santana, J.L. da Silva Junior, D. Noriler, O.P. Taranto, Development of bioactive channels for air treatment with COVID-19 by numerical simulations, Biochem. Eng. J. 224 (2025) 109905, https://doi.org/10.1016/j.bej.2025.109905.
[4] B.F. Leo, C.Y. Lin, K. Markandan, L.H. Saw, M.S. Mohd Nadzir, K. Govindaraju, I. I. Shariffuddin, R. Sankara, Y.W. Tiong, H. Pakalapati, M. Khalid, An overview of SARS-CoV-2 transmission and engineering strategies to mitigate risk, J. Build. Eng. 73 (2023) 106737, https://doi.org/10.1016/j.jobe.2023.106737.
[5] J. Rocklöv, H. Sjödin, A. Wilder-Smith, COVID-19 outbreak on the Diamond Princess cruise ship: estimating the epidemic potential and effectiveness of public health countermeasures, J. Travel Med. 27 (2020) taaa030, https://doi.org/10.1093/jtm/taaa030.
[6] Y. Shen, C. Li, H. Dong, Z. Wang, L. Martinez, Z. Sun, A. Handel, Z. Chen, E. Chen, M.H. Ebell, F. Wang, B. Yi, H. Wang, X. Wang, A. Wang, B. Chen, Y. Qi, L. Liang, Y. Li, F. Ling, J. Chen, G. Xu, Community outbreak investigation of SARS-CoV-2 transmission among bus riders in Eastern China, JAMA Intern. Med. 180 (2020) 1665–1671, https://doi.org/10.1001/jamainternmed.2020.5225.
[7] L. Zhao, Q. Zhou, Z. Wang, A systematic review on modelling the thermal environment of vehicle cabins, Appl. Therm. Eng. 257 (2024) 124142, https://doi.org/10.1016/j.applthermaleng.2024.124142.
[8] S. Khatoon, M. Kim, Human thermal comfort and heat removal efficiency for ventilation variants in passenger cars, Energies 10 (2017) 1710, https://doi.org/10.3390/en10111710.
[9] J.H. Moon, J.W. Lee, C.H. Jeong, S.H. Lee, Thermal comfort analysis in a passenger compartment considering the solar radiation effect, Int. J. Therm. Sci. 107 (2016) 77–88, https://doi.org/10.1016/j.ijthermalsci.2016.03.013.
[10] J. Sip, F. Lizal, J. Pokorny, J. Elcner, J. Jedelsky, M. Jicha, Automotive cabin vent: comparison of RANS and LES approaches with analytical-empirical equations and their validation with experiments using hot-wire anemometry, Build. Env. 233 (2023) 110072, https://doi.org/10.1016/j.buildenv.2023.110072.
[11] S. Sen, M. Selokar, Numerical simulation and validation of cabin aiming and cool-down of a passenger car, SAE Int. J. Passeng. Cars - Mech. Syst. 09 (01) (2016) 2016-01-0251, https://doi.org/10.4271/2016-01-0251.
[12] P. Bandi, N. Paul, M.P. Maiya, S. Tiwari, A. Thangamani, L. Tamalapakula, Influence of flow and thermal characteristics on thermal comfort inside an automobile cabin under the effect of solar radiation, Appl. Therm. Eng. 203 (2022) 117946, https://doi.org/10.1016/j.applthermaleng.2021.117946.
[13] S. Chen, D. Xue, Q. Li, B. Du, X. Fan, Thermal comfort of automobile driver based on local air conditioning vent arrangement, Int. J. Automot. Technol. 24 (2023) 945–954, https://doi.org/10.1007/s12239-023-0077-7.
[14] P. Dancă, A. Jamin, I. Nastase, B. Janssens, W. Bosschaerts, C. Coşoiu, Experimental and numerical study of the flow dynamics and thermal behavior inside a car cabin: innovative air diffusers and human body plumes interactions, Energy Rep. 8 (2022) 992–1002, https://doi.org/10.1016/j.egyr.2022.07.133.
[15] A. Warey, S. Kaushik, B. Khalighi, M. Cruse, G. Venkatesan, Data-driven prediction of vehicle cabin thermal comfort: using machine learning and high-fidelity simulation results, Int. J. Heat Mass Transf. 148 (2020) 119083, https://doi.org/10.1016/j.ijheatmasstransfer.2019.119083.
[16] I. Reda, E.E. Khalil, T.M. Aboudeif, A.E. Degwy, Modeling of thermal comfort in passengers' car cabin, J. Basic Appl. Res. Int. 23 (2017) 81–92.
[17] F. Nabilou, D. Derwein, A. Kirmas, A. Dhake, R. Vogt, L. Eckstein, K. Rewitz, D. Müller, A. Manikin-Based Study of Particle Dispersion in a Vehicle Cabin, Atmos. (Basel). 16 (2025) 116, https://doi.org/10.3390/atmos16020116.
[18] Y. Pan, W. Huang, H.K. Dai, Y. Bian, K.-F. Ho, C. Chen, Evaluation of intervention measures in reducing the driver's exposure to respiratory particles in a taxi with infected passengers, Sci. Total Env. 902 (2023) 166099, https://doi.org/10.1016/j.scitotenv.2023.166099.
[19] F. Arpino, G. Cortellessa, G. Grossi, H. Nagano, A eulerian-lagrangian approach for the non-isothermal and transient CFD analysis of the aerosol airborne dispersion in a car cabin, Build. Env. 209 (2022) 108648, https://doi.org/10.1016/j.buildenv.2021.108648.
[20] F. Arpino, G. Grossi, G. Cortellessa, A. Mikszewski, L. Morawska, G. Buonanno, L. Stabile, Risk of SARS-CoV-2 in a car cabin assessed through 3D CFD simulations, Indoor Air 32 (3) (2022) 1–20, https://doi.org/10.1111/ina.13012.
[21] S. Kim, S. Jung, M. Seyedi, H.-K. Kim, Ventilation efficiency in road vehicles and probability of respiratory infection, Transp. Eng. 12 (2023) 100173, https://doi.org/10.1016/j.treng.2023.100173.
[22] Y. Yan, X. Li, L. Yang, P. Yan, J. Tu, Evaluation of cough-jet effects on the transport characteristics of respiratory-induced contaminants in airline passengers' local environments, Build. Env. 183 (2020) 107206, https://doi.org/10.1016/j.buildenv.2020.107206.
[23] X. Li, Y. Yan, X. Fang, F. He, J. Tu, Towards understanding of inhalation exposure of pilots in the control cabin environment, Build. Env. 242 (2023) 110572, https://doi.org/10.1016/j.buildenv.2023.110572.

[24] C. Qin, K. Zhao, Z. Wang, Z. He, W.-Z. Lu, X. Lyu, X. Gu, Accommodation environment of a polar cruise ship: stratified or mixing ventilation system, Build. Env. 303 (2026) 114975, https://doi.org/10.1016/j.buildenv.2026.114975.
[25] P. Cao, S. Liu, P. Chen, G. Chen, J. Li, Z. Tan, Ventilation strategies for minimizing airborne infection risks inside vehicles: insights from computational modeling, Indoor Air 2025 (1) (2025) 7227486, https://doi.org/10.1155/ina/7227486.
[26] B.E. Yuce, Y.E. Cetin, M. Kriegel, P.V. Nielsen, Integrated assessment of ventilation strategies for exposure and comfort in a multi-bed negative-pressure isolation room, Results Eng 29 (2026) 109210, https://doi.org/10.1016/j.rineng.2026.109210.
[27] N. Choi, M.P. Bivolarova, P. Wargocki, Performance of a prototype of the push-pull type personalized air curtain (PPAC) aimed to reduce respiratory infection risks, Build. Env. 282 (2025) 113314, https://doi.org/10.1016/j.buildenv.2025.113314.
[28] ANSYS Inc., Ansys Fluent Theory Guide, Release 2025 R1, ANSYS Inc., Canonsburg, PA, 2025.
[29] T. Liu, Y. Guo, X. Hao, M. Wang, S. He, Z. Lin, R. Zhou, Evaluation of an innovative pediatric isolation (PI) bed using fluid dynamics simulation and aerosol isolation efficacy, Build. Simul. 14 (2021) 1543–1552, https://doi.org/10.1007/s12273-021-0761-3.
[30] P.V. Nielsen, C. Xu, Multiple airflow patterns in human microenvironment and the influence on short-distance airborne cross-infection - A review, Indoor Built Env. 31 (2022) 1161–1175, https://doi.org/10.1177/1420326X211048539.
[31] J. Ma, X. Qi, H. Chen, X. Li, Z. Zhang, H. Wang, L. Sun, L. Zhang, J. Guo, L. Morawska, S.A. Grinshpun, P. Biswas, R.C. Flagan, M. Yao, Coronavirus disease 2019 patients in earlier stages exhaled millions of severe acute Respiratory syndrome Coronavirus 2 per hour, Clin. Infect. Dis. 72 (2021) e652–e654, https://doi.org/10.1093/cid/ciaa1283.
[32] R.S. Papineni, F.S. Rosenthal, The size distribution of droplets in the exhaled breath of healthy human subjects, J. Aerosol Med. 10 (1997) 105–116, https://doi.org/10.1089/jam.1997.10.105.
[33] M. Bivolarova, J. Ondráček, A. Melikov, V. Ždímal, A comparison between tracer gas and aerosol particles distribution indoors: the impact of ventilation rate, interaction of airflows, and presence of objects, Indoor Air 27 (2017) 1201–1212, https://doi.org/10.1111/ina.12388.
[34] X. Li, J. Niu, N. Gao, Spatial distribution of human respiratory droplet residuals and exposure risk for the co-occupant under different ventilation methods, HVAC&R Res 17 (2011) 432–445, https://doi.org/10.1080/10789669.2011.578699.
[35] X. Li, J. Niu, N. Gao, Co-occupant's exposure to exhaled pollutants with two types of personalized ventilation strategies under mixing and displacement ventilation systems, Indoor Air 23 (2013) 162–171, https://doi.org/10.1111/ina.12005.
[36] D.K. Milton, A Rosetta stone for understanding infectious drops and aerosols, J. Pediatr. Infect. Dis. Soc. 9 (2020) 413–415, https://doi.org/10.1093/jpids/piaa079.
[37] F. Bode, T. Joldos, G.M. Sirbu, P. Danca, I. Nastase, C. Coşoiu, Impact of realistic boundary conditions on CFD simulations: A case study of vehicle ventilation, Build. Env. 267 (2025) 112264, https://doi.org/10.1016/j.buildenv.2024.112264.
[38] G. Grossi, F. Arpino, M. Bertone, G. Cortellessa, A. Sciacchitano, On the effectiveness of Reynolds-averaged and subgrid scale models in predicting flows inside car cabins, Phys. Fluids 36 (2024) 015137, https://doi.org/10.1063/5.0180823.
[39] L.D. Knibbs, R.J. de Dear, S.E. Atkinson, Field study of air change and flow rate in six automobiles, Indoor Air 19 (4) (2009) 303–313, https://doi.org/10.1111/j.1600-0668.2009.00593.x.
[40] S.A. Fruin, N. Hudda, C. Sioutas, R.J. Delfino, A predictive model for vehicle air exchange rates based on a large, representative sample, Env. Sci. Technol. 45 (2011) 3569–3575, https://doi.org/10.1021/es103897u.
[41] S. Daly, Automotive Air-conditioning and Climate Control Systems, Butterworth-Heinemann, Oxford, 2006.
[42] D.D. Gray, A. Giorgini, The validity of the boussinesq approximation for liquids and gases, Int. J. Heat Mass Transf. 19 (1976) 545–551, https://doi.org/10.1016/0017-9310(76)90168-X.
[43] M. Kiliç, G. Sevilgen, The effects of using different type of inlet vents on the thermal characteristics of the automobile cabin and the human body during cooling period, Int. J. Adv. Manuf. Technol. 60 (2012) 799–809, https://doi.org/10.1007/s00170-011-3594-x.
[44] V. Adhikari, A. Nassar, Q. Nagpurwala, Numerical studies on the effect of cooling vent setting and solar radiation on air flow and temperature distribution in a passenger car. SAE Tech. Pap. 2009-28-0048, 2009, https://doi.org/10.4271/2009-28-0048.
[45] J.P. Rugh, D. Bharathan, Predicting Human thermal comfort in automobiles, SAE Trans 114 (2005) 2508–2516, https://doi.org/10.4271/2005-01-2008.
[46] REHVA, REHVA COVID-19 guidance document, how to operate HVAC and other building service systems to prevent the spread of the coronavirus (SARS-CoV-2) disease (COVID-19) in workplaces, Fed, Eur, Heat. Vent, Air Cond, Assoc, (2020).
[47] G. Buonanno, L. Stabile, L. Morawska, Estimation of airborne viral emission: Quanta emission rate of SARS-CoV-2 for infection risk assessment, Env., Int, 141 (2020) 105794, https://doi.org/10.1016/j.envint.2020.105794.
[48] P.O. Fanger, A.K. Melikov, H. Hanzawa, J. Ring, Turbulence and draft, ASHRAE J 31 (1989) 18–25.
[49] ISO 7730:2025, Ergonomics of the thermal environment - Analytical determination and interpretation of thermal comfort using calculation of the PMV and PPD indices and local thermal comfort criteria, International Organization for Standardization, Geneva, 2025.
[50] Y. Ozeki, J.H. Yang, H. Nagano, S. Kato, E. Nomura, M. Inoue, S. Kobayashi, Ventilation characteristics of modeled compact car part 1 airflow velocity measurement with PIV, SAE Tech. Pap. 1 (1) (2009) 631–639, https://doi.org/10.4271/2008-01-0732.
[51] N. Arslanoglu, A. Yigit, Investigation of efficient parameters on optimum insulation thickness based on theoretical-Taguchi combined method, Env., Prog, Sustain, Energy 36 (2017) 1824–1831, https://doi.org/10.1002/ep.12628.
[52] B.E. Yuce, P.V. Nielsen, P. Wargocki, The use of Taguchi, ANOVA, and GRA methods to optimize CFD analyses of ventilation performance in buildings, Build, Env., 225 (2022) 109587, https://doi.org/10.1016/j.buildenv.2022.109587.
[53] N. Arslanoglu, A. Yigit, Experimental investigation of radiation effect on human thermal comfort by Taguchi method, Appl. Therm. Eng. 92 (2016) 18–23, https://doi.org/10.1016/j.applthermaleng.2015.09.070.
[54] H. Bayram, Analysis of numerical and grey relation method of the effect of helical tape insert density on the hydrothermal performance, Case Stud, Therm. Eng. 39 (2022) 102406, https://doi.org/10.1016/j.csite.2022.102406.
[55] T. Ležovič, F. Lízal, J. Jedelský, M. Jícha, HVAC automotive vents evaluation and their performance, HVAC&R Res 19 (2013) 1073–1082, https://doi.org/10.1080/10789669.2013.824498.